Low-frequency noise spectroscopy as an effective tool for electric transport analysis

Costantino Mauro

A Dissertation submitted to the

Dipartimento di Fisica "E.R. Caianiello"
Facoltà di Scienze Matematiche Fisiche e Naturali

in fulfillment of the requirements
for the

Doctoral degree in Physics

in the

Università degli Studi di Salerno

under the Supervision of

Prof. Sergio Pagano

Doctoral Student XXX Cycle (2015–2017)
Head of the School: Prof. R. Scarpa

"Books are a way of being fully human"

Susan Sontag

Contents

INTRODUCTION

It is a notable fact of nature that processes varying with time in an extremely complicated way often lead to observable averages that follow simple laws: the fast irregular collision of a piston by gas molecules, when integrated by the inertia of the piston, causes the piston to move smoothly in a motion described by Boyle's law. Similarly, the instantaneous current fluctuations in a resistive circuit average out to Ohm's law. The intensity of these fluctuations depends on materials, device type, its manufacturing process, and operating conditions. Noise, that is fluctuation is a manifestation of the thermal motion of matter and discreteness of its structure [1]. For example, in a circuit having a potential barrier such as a rectifying junction in a diode, the current is restricted to those electrons that have sufficient thermal energy to surmount the barrier. As a result, the current fluctuates in a way that is determined by the thermal fluctuations in the position and energy distribution of the electrons, producing a particular noise, called shot noise.

The introduction of the concept of noise and development of the physics of fluctuations is one of the conquest of twentieth-century physics. The early steps date back to '20s of XIX century. The English botanist Robert Brown, under microscope, observed the endless dance of pollen particles in aqueous suspension. The same happened later with mineral and smoke particles.

Only the kinetic theory of gases, in the latter part of the nineteenth century, correctly explained the Brownian movement as thermal molecular motions in the liquid environment of the particles. Moreover, the quantitative description of the Brownian motion of a particle was resolved in 1905 by Einstein.

Over time, physicists have developed special techniques for dealing with the way in which these macroscopic regularities arise from microscopic systems. For example, a monatomic gas in a cylinder is completely determined if the three position coordinates and the three momentum coordinates are specified for each of the N molecules at some instant called the initial time.

The basic idea of statistical mechanics is to replace the evolving system by an appropriate ensemble of systems, abide by the same equations of motion but having different initial microstates x.

The investigation of fluctuation phenomena, which may be called "fluctuation spectroscopy", is a valuable tool for the study of kinetic processes in matter, often much more sensitive than the measurement of mean quantities. The required measurement instrument, i.e. the "magnifier" companion is the spectrum analyzer, which acts as a microscope: it enables the visualization and measuring of voltage fluctuations, giving information on the conduction mechanisms and the dynamic behaviors of the charge carriers in the investigated systems.

In this work, several experiments and analyses performed on a broad typology of materials and compounds are presented. Structural, DC electrical

transport and noise properties are exposed for each investigated sample, and theoretical models and possible explanations of the experimental results are given to unravel physical phenomena. In particular, in Chapter 2, two distinct types of iron-chalcogenide superconductors are investigated, in their pristine and aged state, suggesting the more likely mechanism which generates the resistance fluctuations and resorting to Weak Localization theory. In Chapter 3, for the polymer/carbon nanotubes composites, the fluctuation-induced tunneling model is introduced to explain the measured temperature dependence of the electrical conductance and the I-V curve behaviors. The model can be also used to describe the resistance fluctuation processes (noise), confirming the dominant role of the intergranular tunneling processes [1]. In Chapter 4, noise spectroscopy is the swiss knife for the extraction of several parameters, which are then applied to a noise model for the evaluation of defect states in silicon based solar cells. In Chapter 5, the recombination kinetics in polymer:fullerene solar cells are investigated, shading light on the influence of the solvent additives on the temperature behavior of charge carrier transport. In the last chapter, noise measurements prove the existence of a structural phase occurring within the perovskite compound and highlight the correlation between electronic defect states distribution and device performance.

All the experiments and the noise measurements were carried out in the laboratory of the Physics Department, University of Salerno, Fisciano (Italy), under the supervision of the Prof. Sergio Pagano and Dr. Carlo Barone.

CHAPTER I
Noise theory: a brief overview

Noise or fluctuations are spontaneous stochastic (random) variations of physical quantities in time, that is, random deviations of these quantities from some mean values that are either constant or evolve nonrandomly in time. Then, it is clear that noise is a random *process*. For example, the random character of the fluctuations in solids is a consequence of the fact that thermal motion and quantum transition of particles (electrons and atoms) are random.

Being noise a stochastic phenomenon, it is necessary to deal with probability, its concepts, properties and mathematical tools.

By definition, a random process is a random function *x(t)* of an independent variable *t*, representing the time.

The distribution function of the n-th order for the given random process *x(t)* is defined as

$$W_n(x_1,t_1;\ldots;x_n,t_n) = P\{x(t_1) \le x_1;\ldots;x(t_n) \le x_n\} \tag{1.1}$$

whit x_i the value of the random quantity at the time t_i, and *P{...}* the probability of the considered event, indicated in the curly brackets.

Under the hypothesis that $W_n\,(x_1\,,\,t_1;\ldots.;\,x_n\,,\,t_n)$ are differentiable functions of the variables x_1 ,...., x_n, the corresponding probability density functions can be defined as

$$w_n(x_1,t_1;\ldots;x_n,t_n) = P\left\{x_1 \le x(t_1) < x_1 + dx_1;\ldots;x_n \le x(t_n) < x_n + dx\right\} \tag{1.2}$$

The first-order central moment (i.e. the mean value) of the random variable *x(t)* is e expressed as

$$\langle x(t)\rangle = \int_{-\infty}^{+\infty} x(t)dW(x) = \int_{-\infty}^{+\infty} dx\, x w_1(x,t)\,. \tag{1.3}$$

Following, the second-order central moment is the variance (i.e., the mean value of the fluctuation squared). The r-th order central moment is the average value of the random quantity $(\delta x(t))^r$, whit $\delta x(t) = x(t) - \langle x\rangle$ the deviation of the random quantity $x(t)$ from its mean value $\langle x\rangle$, that is the fluctuation

$$\langle[\delta x(t)]^r\rangle = \int_{-\infty}^{+\infty} dx(\delta x)^r\, w_1\left(x,t\right). \tag{1.4}$$

At this point, a useful concept can be introduced: the correlation function. If the probability density $w_n\,(x_1\,,\,t_1;\ldots;\,x_n\,,\,t_n)$ is known for different times $t_1\,,\ldots,\,t_n$, the correlation function can be computed as

$$\langle \delta x(t_1)\ldots\delta x(t_n)\rangle = \int dx_1 dx_2\ldots dx_n \delta x_1\ldots\delta x_n w_n(x_1,t_1;\ldots;x_n,t_n) \tag{1.5}$$

It is one of the distinctive sign of a random process since it is a nonrandom property of the kinetics of the random fluctuations: it describes how the fluctuations $\delta x(t)$ evolve in time on average.

A fundamental distribution is the Gaussian (i.e. normal) distribution, which can be considered when the random quantity *x(t)* is a sum of many independent and evenly distributed random quantities.

Let $\xi_1,\ldots\xi_N$ be independent and identically distributed random quantities and let $x = \xi_1 +\ldots+ \xi_N$. Let the terms $\xi_1,\ldots\xi_N$ be small enough while their number *N* be great enough (ideally $N \longrightarrow \infty$), then the mean value of *x(t)* is equal to $\langle x\rangle$, and the variance of *x(t)* is equal to σ^2, the 1-dimensional probability density function is

$$w_1(x) = \frac{1}{\sqrt{2\pi\sigma^2}}\exp\left[-\frac{(\delta x)^2}{2\sigma^2}\right] \tag{1.6}$$

where $\delta x = x - \langle x\rangle$ is the fluctuation. This kind of distribution is called Gaussian or normal. A random process is defined as Gaussian when all its probability density functions are normal for all $n = 1$. The n-dimensional normal distribution is

$$w_n(x_1,\ldots,x_n) = \frac{1}{\sqrt{(2\pi)^n \det\hat{\lambda}}}\exp\left[-\frac{1}{2}\sum_{i=1}^{n}\sum_{j=1}^{n}\lambda_{ij}^{-1}\delta x_i \delta x_j\right] \tag{1.7}$$

where $\delta x_i = x_i - \langle x_i\rangle$, and $\hat{\lambda}$ is the covariance matrix and its elements equal $\lambda_{ij} = \langle \delta x_i \delta x_j\rangle = \lambda_{ji}$.

By taking into account Eq. (1.5) and (1.7), for Gaussian random processes, all nonzero n-th order ($n > 2$) moments can be expressed in terms of the second-order moments, that is the covariances λ_{ij}. This mean that the study of higher-order correlations is not able to give any new information apart from that which is contained in the covariance.

In this case, Eq. (1.5) can be expressed in terms of the two-dimensional probability density

$$\psi_x(t_1,t_2) = \int dx_1 dx_2 \delta x_1 \delta \mathrm{x}_2 w_2(x_1,\mathrm{t}_1;x_2,\mathrm{t}_2) \tag{1.8}$$

where $\delta x_1 = x_1 - \langle x(t_1)\rangle$, $\delta x_2 = x_2 - \langle x(t_2)\rangle$. At a closer look, Eq. (1.8) represent the correlation between the values of the random process at two different times, and is mostly known as the autocorrelation function.

If all distributions $w_n\,(x_1\,,\,t_1\,;\ldots;\,x_n\,,\,t_n)$ stay identical under any identical shift of all times instants $t_1;\ldots;\,t_n$, the associated random process is called stationary.

Therefore, for a stationary process the probability density function $w_1\,(x_1,\,t_1)$ does not depend on the instant t_1, so that the probability density function $w_2\,(x_1\,,\,t_1;\,x_2\,,\,t_2)$ depends only on the difference $t_1 - t_2$.

The properties of a stationary random process can be often described, by computing time averages over specific sample functions in the ensemble. The autocorrelation function is also determined by averaging over a sufficiently long time of observation t_m

$$\Psi_x(t_1-t_2) = \lim_{t_m\to\infty}\frac{1}{t_m}\int_{-t_m/2}^{t_m/2} dt\,\delta x(t_1+t)\delta x(t_2+t) \tag{1.9}$$

It is worth noting both autocorrelation functions (1.8) and (1.9) equal when the system is ergodic, i.e., all the time-averaged properties are equal to the corresponding ensemble averaged values [1]. The good news are that random data representing stationary physical phenomena are usually ergodic.

If the autocorrelation is the main statistical function used to describe the basic properties of random data in the time domain, the spectral density function ($S_x(f)$), which is the Fourier transform of the autocorrelation function, gives similar information in the frequency domain. By applying the Wiener-Khintchine theorem [1], it follows that

$$s_x(f) = 2\int_{-\infty}^{+\infty} d(t_1-t_2)e^{-i\omega(t_1-t_2)}\Psi_x(t_1-t_2) \equiv 2\Psi_x(\omega) \tag{1.10}$$

or rather,

$$\langle(\delta x)^2\rangle = \Psi_x(t_1-t_2=0) = \int_0^{+\infty} S_x(f)\,df \tag{1.11}$$

In a graceful way, Eq. (1.11) expresses that the integral of the spectral density over all positive frequencies is exactly the variance of the noise.

1.1 Noise spectral density measurements

Figure 1.1 shows a typical spectral density S_V of voltage fluctuations processes in a crystalline silicon-based solar cell as a function of the frequency.

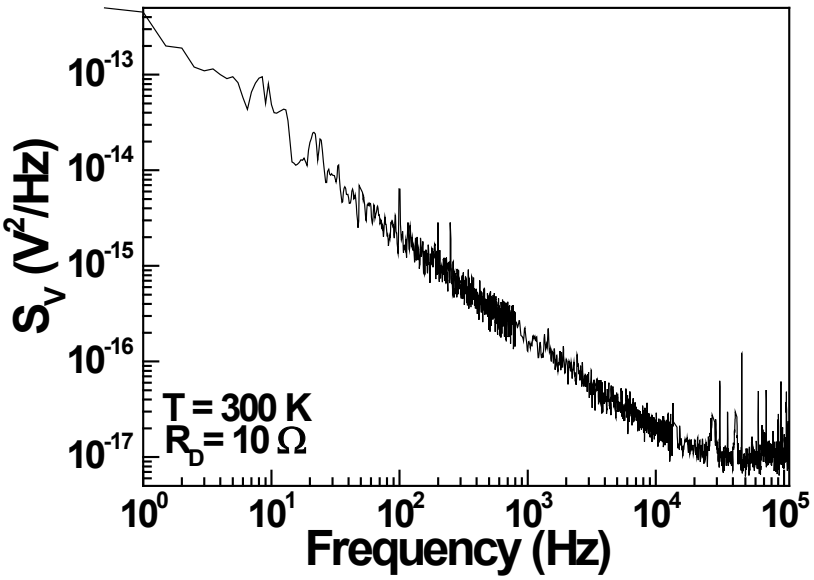

Figure 1.1 Spectral density as a function of the frequency for a silicon-based solar cell at temperature T = 300 K and at a differential resistance R_D = 10 ohm in dark condition.

Two distinct voltage noise components can be recognized, so that the spectral density S_V can be regarded as the sum of two terms, $S_V = S_{V_1} + S_{V_2}$.

The first component can be expressed by

$$S_{V_1}(f) = \frac{K}{f^{\alpha}} \tag{1.12}$$

with f the frequency, K the temperature-dependent noise amplitude and α the temperature-dependent frequency exponent.

In particular, the value of α is usually close to unity. This feature justifies the term *1/f* noise. For example, in continuous metal film and in carbon resistor, the value of α averaged over many specimen stands around 1 with very small variations.

The second component has spectral density given by

$$S_{V_2}(f) = const \tag{1.13}$$

not dependent on frequency.
This term takes into account noise components that are associated generally to two distinct mechanisms [1]:

- temperature fluctuation processes (Johnson noise), having spectral density expression given by

$$S_V^{JN} = 4k_B TR \tag{1.14}$$

where k_B is Boltzmann's constant, T is the system temperature, and R is the real part of the system impedance;
- current fluctuation processes (shot noise), having spectral density expressed by

$$S_V^{SN} = 2eR_D^2 I \tag{1.15}$$

whit e the electron charge and R_D the differential resistance of the system.
In the current thesis, the power spectral density function measurement will allow to extricate the frequency composition of the data, unravelling the basic characteristics of the physical system involved.

1.2 Noise and electrical dc measurements: experimental setup

All the measurements have been carried out in a closed-cycle cold finger ^{4}HE gas refrigerator. The cold finger cooling head is sealed in a vacuum jacket, and the thermal isolation is assured both by medium vacuum ($5x10^{-4}$ mbar) and by a radiation shield. The temperature has been stabilized using a GaAlAs thermometer and a resistance heater. The sample temperature has been monitored by a Cernox resistor thermometer fastened to the sample holder. Resistance measurements have been taken in current-pulsed mode and the voltage drop has been measured with a digital multimeter. The investigated samples have been biased with a programmable dc current source and a voltage compliance of up to 105 V. Current-Voltage measurements have been carried out using current pulses too, and response voltage has been measured by a spectrum analyzer in time domain or alternatively by a digital nanovoltmeter. The noise measurements have been performed by amplifying the voltage signal with a Signal Recovery PAR5113 preamplifier and by analyzing with a Hewlett Packard dynamic signal analyzer model 35670A (see Fig. 1.2).

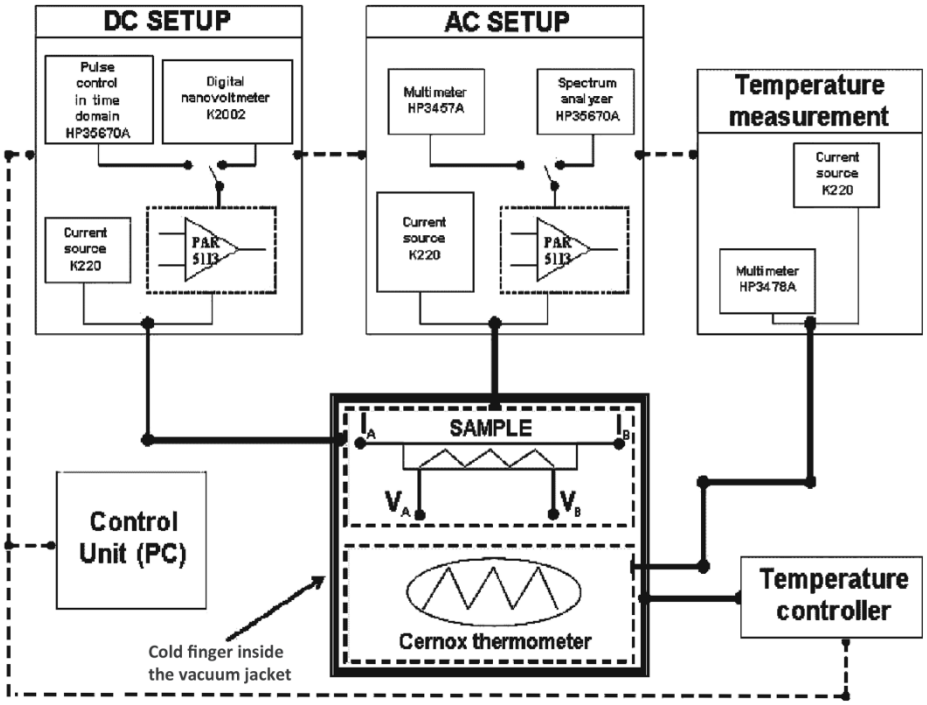

Figure 1.2 Schematic view of the experimental setup.

The number of acquired traces are usually more than 100. This number is a good compromise between the introduced error (<10%) and the time spent for each measurement. The equivalent input voltage noise density of the electronic chain is typically $SV_n \approx 1.4 \times 10^{-17}$ V^2/Hz in the range [1 – 10^6] Hz with a *1/f* rise below 1 Hz.

The software for the data acquisition, logging, and visualization has been developed in the LabVIEW environment. Four different programs have been written for: system temperature setting and controlling; R(T) curves acquisition; I-V curves acquisition; voltage spectral density traces acquisition.

The system temperature is set and stabilized with the PID (Proportional-Integral-Derivative) algorithm, which attempts to correct the error between a measured process variable and a desired setpoint by calculating and then outputting a corrective action that can adjust the process accordingly. The temperature resolution is below 0.1 K.

Concerning the spectral noise acquisition, the programmed LabVIEW interface allows to set several bias current values and several frequency ranges, with different averaging numbers for each one (see Fig. 1.3).

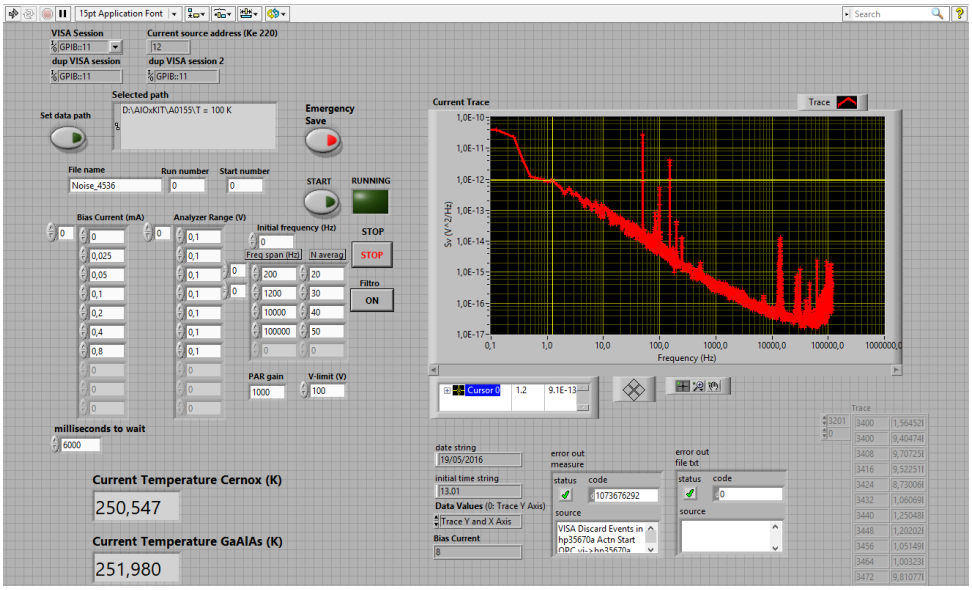

Figure 1.3 Control panel of the LabVIEW program dedicated to the noise spectral density acquisition. Several frequency ranges, numbers of averages and bias current value can be set.

The program acquires two different temperature values, too: one from the GaAlAs thermometer, that is the cold finger temperature, the other value coming from the Cernox thermometer, attached to the sample holder.

The investigated samples have been contacted with the four-point, or Kelvin, probe method, that is the most common way to measure the resistance of a conducting material. This technique consists of two current carrying probes (the two outer contacts) and two voltage measuring probes (the two inner contacts). This arrangement eliminates measurement errors due to the probe resistance, and the contact resistance between each metal probe and the specimen material. More in details, the contact resistance refers to the contribution to the total resistance of a material which comes from the electrical leads and connections, as opposed to the intrinsic resistance which is an inherent property, independent of the measurement method. In the simple two-probe method, the measurement current causes a potential drop across both the test leads and the contacts so that the introduced parasitic resistance cannot be separated from the resistance of the device under test.

CHAPTER 2
Noise properties and transport in aging-induced degraded iron-based superconductors

Iron-based superconductors constitute a relevant discovery in the field of condensed matter physics. At the core of this family of compounds, iron-chalcogenides are considered ideal systems to better understand the transport and superconducting mechanisms, thanks to their simple chemical and crystallographic structure. In addition, a renovated interest on these materials has been registered, due to the recent observation of a superconducting transition above 100 K in FeSe films grown on $SrTiO_3$ substrates [2].

The nature of superconductivity in iron-chalcogenides is still unclear, so that the study of the charge transport by means of noise spectroscopy could improve the knowledge about iron-based superconductors behavior. For this purpose, thermal and voltage activated excess *1/f* noise has been associated to nonlinear conductivity fluctuations in Fe(Se,Te) thin films [3] previously.

Iron-based superconductors are prone to degradation when exposed to unprotected environmental conditions, with a very likely vanish of their superconductive properties. The understanding of aging effects is of interest in view of practical applications. In this respect, voltage-noise and electric transport measurements have been carried out on FeSe and $FeSe_{0.5}Te_{0.5}$ thin films, just after fabrication and after long aging in protected environment. The uncontaminated films exhibit a superconducting transition at temperatures ranging from 9 to 12 K for FeSe and at 17 K for $FeSe_{0.5}Te_{0.5}$, and an overall metallic behavior above T_c. Preserving the samples for several months in low-humidity and low-pressure conditions, the $FeSe_{0.5}Te_{0.5}$ films does not show evident modification of the electrical conduction mechanisms. Conversely, the superconductive transition is no longer present in the FeSe films, at least for temperatures above 8 K, and an overall larger resistivity is observed, with a characteristic upturn at low temperatures ($T < T_{min} \approx 50$ K).

2.1 Materials and methods

The investigated films were prepared at the Department of Basic Science, University of Tokyo (Japan) by a pulsed KrF laser deposition. The targets were made of polycrystalline pellets of FeSe and of $FeSe_{0.5}Te_{0.5}$, while commercial single crystals of CaF_2 (100) were used as substrates [4]. The optimal deposition parameters, that is substrate temperature, back pressure, and laser beam repetition rate were: 7 K, 10^{-6} Torr, and 10 Hz, for FeSe; 7 K, 10^{-7} Torr and 20 Hz

for $FeSe_{0.5}Te_{0.5}$. The film thickness, ranging from 15 to 148 nm, was measured using a Dektak 6-M stylus profiler. Four-circle X-ray diffraction (XRD) with Cu Kα radiation at room temperature was used to identify the crystal structure, indicating a good c axis film orientation [4].

The samples were patterned in an eight-terminal shape, by means of a metal mask, in order to obtain well defined geometries (see Fig. 2.1). Two equivalent types of electric contacts were used: wire bonding with silver paste, and mechanically pressed indium pads using a custom-made sample holder (see Fig. 2.1 for details).

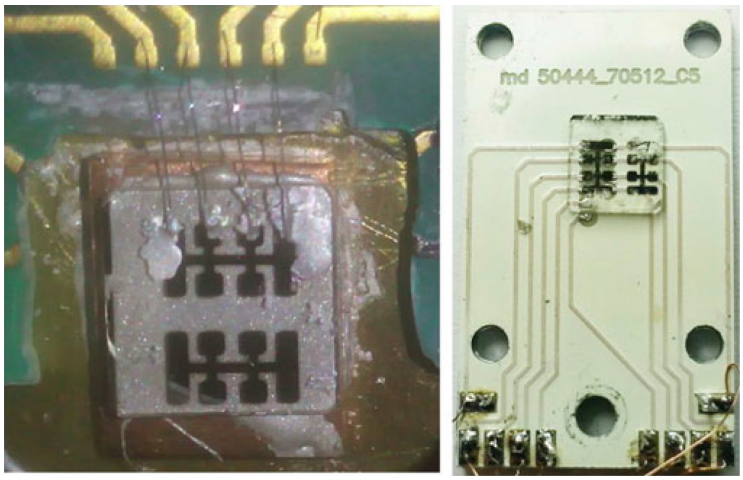

Figure 2.1 Wire bonding contacted FeSe sample (left panel) and contacted $FeSe_{0.5}Te_{0.5}$ sample by mechanically pressed indium pads on custom-made sample holder (right panel).

The latter was designed by the author with a PCB-CAD software, then manufactured on aluminium-ims (insulated metal substrate) which provides an optimal thermal conduction.

All the measurement were carried out by using the experimental setup described in the chapter 1.

2.2 DC electrical transport properties

Resistance versus temperature data has been measured in current-pulsed mode by biasing the samples with a current of 50 μA. The graphs depicting the resistance trends are shown in Fig. 2.2.

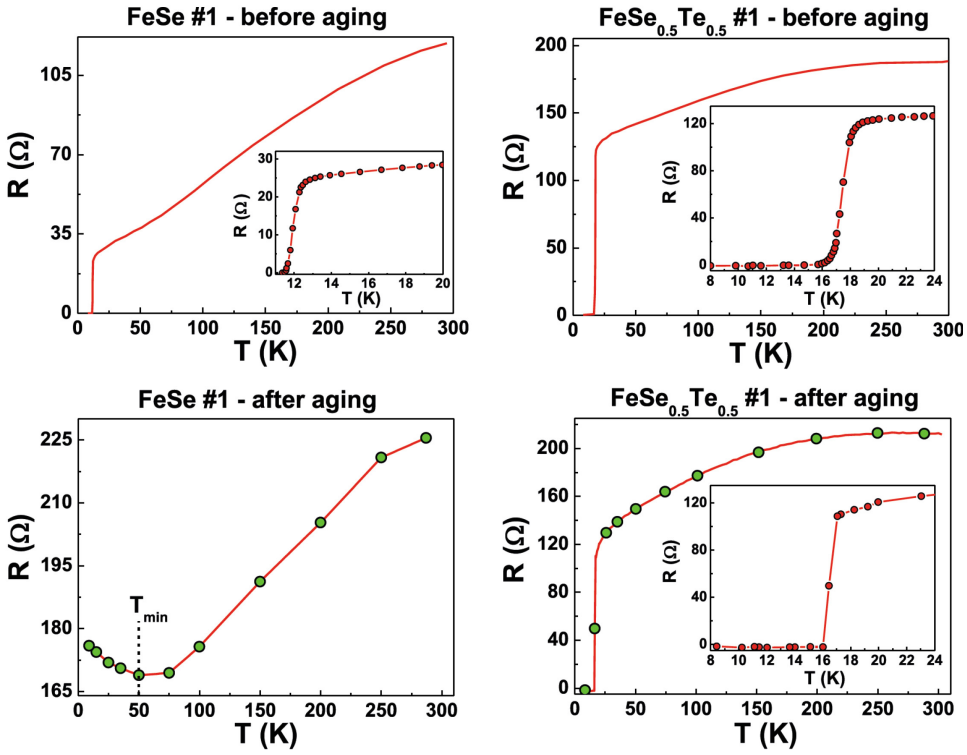

Figure 2.2 Temperature dependence of the sample resistance R of FeSe and $FeSe_{0.5}Te_{0.5}$ (left and right panels, respectively), before and after aging (upper and lower panels, respectively). Green circles represent the temperatures, at which noise measurements have been performed.

Just after fabrication, the investigated samples show a superconducting transition, defined as 50% of normal state resistance, at a temperature T_c = 12.0 K for FeSe and T_c = 17.5 K for $FeSe_{0.5}Te_{0.5}$. After aging for several months in protected atmosphere, the two Fe-based films are measured again and show a different behavior. As visible in the lower panels of Fig. 2.2, the $FeSe_{0.5}Te_{0.5}$ film has preserved its transport properties with slight modification. A little increase of resistivity and a small decrease of the critical temperature from 17.5 K to 16 K are observed. Conversely, the FeSe sample does not show the pristine superconducting transition (at least for temperatures above 8 K), and the lowest explored temperature range exhibits an overall larger resistivity with a characteristic upturn at $T < T_{min} \approx 50$K. At a first glance, these experimental findings suggest that the Te substitution into Se sites contribute to enhance T_c and also make the compound more stable.

2.3 Noise spectral density measurements

In order to obtain a more clear picture of the conduction properties, a detailed electric noise characterization of the samples has been performed for several bias currents and temperatures. Both of them, before and after aging, exhibit the same frequency dependence of the voltage-spectral density S_v. In particular, in the range from few Hz to 10^5 Hz, the noise amplitude is characterized by a *1/f* behavior, followed by a constant value at higher frequencies, due to the instrumentation electronic readout and to the sample Johnson noise contributions. Captured spectral traces are shown in Fig. 2.3 at a fixed temperature of 250 K, for the FeSe (left panel) and the $FeSe_{0.5}Te_{0.5}$ (right panel) thin films.

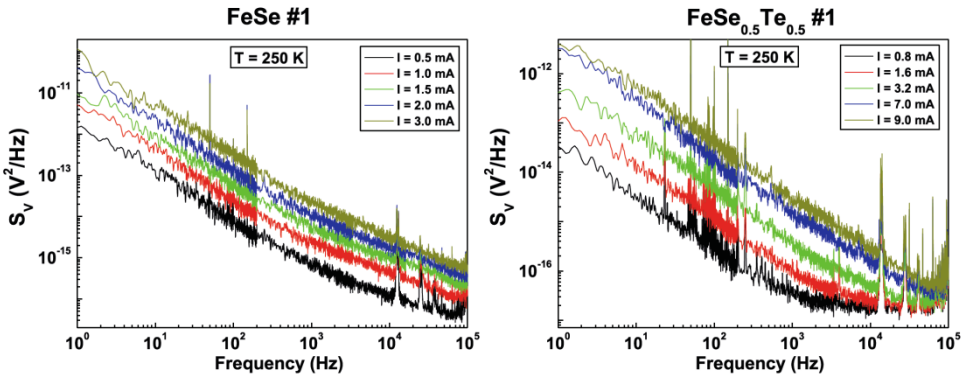

Figure 2.3 Frequency dependence of the voltage-spectral density S_v, acquired at a reference temperature of 250 K and for different bias current values, of FeSe and $FeSe_{0.5}Te_{0.5}$ samples (left and right panels, respectively).

The experimental voltage-spectral densities suggest, therefore, the use of the Hooge relation [1],

$$S_V(f,I,T) = \frac{K_0(T)}{f^{\gamma(T)}} I^{\eta(T)} + C \qquad (2.1)$$

where, K_0 is temperature-dependent noise amplitude, γ and η are the temperature-dependent frequency and current exponents, respectively, and C is the white noise contribution.

In this contest, it could be of help to evaluate the best fitting values for the parameters of Eq. (2.1). They have been calculated and reported in Fig. 2.4.

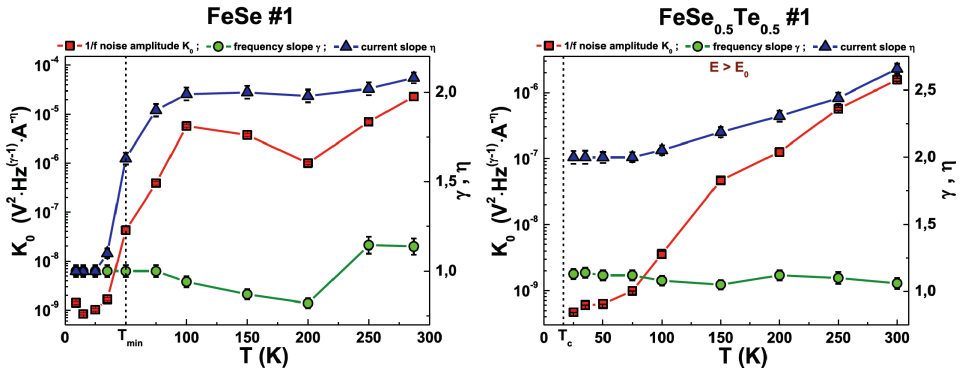

Figure 2.4 Temperature dependence of the fitting noise parameters: amplitude K_0 (left y-axis), frequency slope γ and current slope η (right y-axis). The data for FeSe and $FeSe_{0.5}Te_{0.5}$ samples, after aging, are shown in the left and right panels, respectively.

The value of γ ranges between 0.8 and 1.2 for all the investigated temperatures and samples after aging. This clearly indicates that the dominant noise component is of *1/f*-type [1]. A monotonic increase of K_0 , with the temperature, is observed for the $FeSe_{0.5}Te_{0.5}$ system while FeSe aged films show an evident change of the noise properties below the crossover temperature T_{min}.

The $FeSe_{0.5}Te_{0.5}$ compound is characterized by an electric field threshold E_0 , above which a nonlinear excess noise is activated as proved by the parameter η, displayed in the right panel of Fig. 2.4 as blue triangles, whose value exceeds 2 at temperatures higher than 100 K. This behavior is not observed in the low-temperature region, where standard resistance fluctuations are the noise source, and it has been attributed to the presence of a structural transition near 100 K [5].

2.3.1 Weak-localization effects

The induced degradation of FeSe thin films produces an increase in the resistivity below T_{min}, as clearly showed in Fig. 2.2. This characteristic feature, already reported in scientific literature, is the sign of weak-localization (WL) effects. It has been demonstrated that nonequilibrium universal conductance fluctuations occur in the WL regime causing the linear bias current dependence of the *1/f* noise component [6]. A further proof is given by the temperature dependence of η, as shown in Fig. 2.4 (left panel).

To gain a better picture of the phenomena, It may be worth investigating the nature of these quantum interference effects by analyzing the resistance values near T_{min}. The $R(T)$ curve could be described by using a 2D WL model or a 3D WL model [7] (see Fig. 2.5).

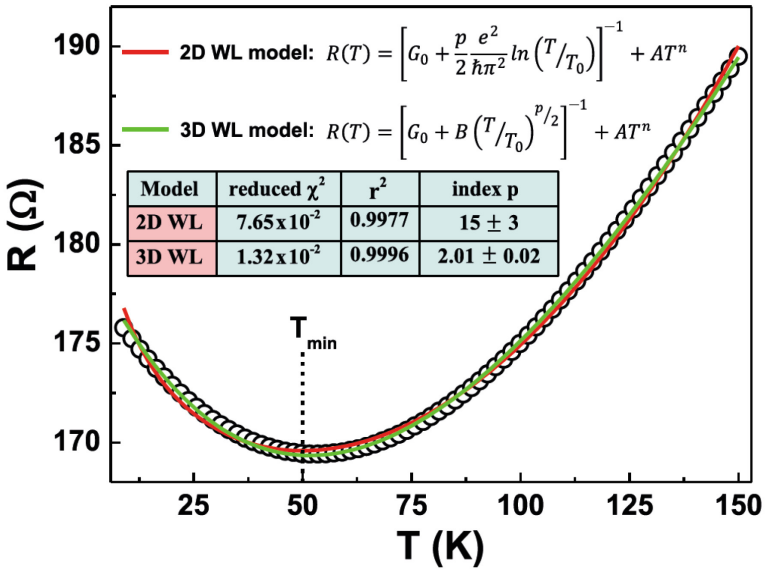

Figure 2.5 The low-temperature resistance of a typical degraded FeSe sample, is reproduced in terms of a 2D WL model (red curve) and of a 3D WL model (green curve). The relevant statistical parameters and the best fitting values of the characteristic index *p* are reported in the inset.

The distinctive parameter is the index *p*, which estimates are 3/2, 2, and 3, depending on whether the inelastic scattering rate is determined by Coulomb interactions in the dirty limit, in the clean limit, or by electron-phonon scattering [7]. Therefore, taking a look at the inset of the Fig. 2.5, the 3D WL model only results to be consistent by a physical point of view: It is characterized by an index *p* close to 2, by the highest coefficient of determination r^2 and by the lowest reduced χ^2. The index *p* value suggests that Coulomb interactions in the clean limit determine the inelastic scattering rate.

To sum up, aging-induced degradation involve different effects in FeSe and $FeSe_{0.5}Te_{0.5}$ samples. While the presence of Te seems to enhance T_c , and to stabilize the compound, completely different dc and ac behaviors are found in pristine and aged FeSe thin films. In particular, the superconducting transition vanishes with sample degradation, and an upturn of the resistivity is observed below a crossover temperature of 50 K. The *1/f* noise component shows an unusual bias current dependence in the low-temperature region, with a clear shift from a quadratic to a linear trend. This experimental evidence corresponds to the occurrence of nonequilibrium universal conductance fluctuations, and is the distinctive feature of weak-localization effects. The weak-localization theory proves the presence of aging-induced scattering centers in the FeSe compound by modeling the low-temperature resistance. The 3D WL model only provides coherent physical parameters from which information on the dimensionality and the type of scattering mechanism can be gathered.

Author contribution The author performed the *R(T)* and voltage noise-measurements of all devices. The author designed the custom-made sample holder by means of a CAD software.

CHAPTER 3
Noise properties and transport in different polymer/carbon nanotube composites

The importance of Carbon nanotubes (CNTs) has grown over time, having novel properties that make them potentially useful in a wide variety of applications in nanotechnology, electronics, optics and other fields of materials science. A carbon nanotube is a tube-shaped material, made of carbon, with a diameter on the nanometer scale. CNTs exhibit extraordinary stiffness and unique electrical properties, and are efficient conductors of heat.

For the realization of CNT based transistors, single-wall carbon nanotubes (SWCNTs) are the best solution. Recently thin film transistors (TFTs) made from networks of semiconductor-enriched SWCNTs have reached performances that outperform the commercial state-of-the-art thin film transistor technologies [8]. Conversely, Multi-wall carbon nanotubes (MWCNTs) generally have metallic behavior that play an important role as transparent conductive contacts for RF-shielding, for solar cells and as sensors and actuators.

Electrical noise is typically a limiting factor for the functionality of electronic devices and sensors. While many studies inspect the noise behavior of devices prepared with SWCNTs, fewer reports on noise characteristics of MWCNT composites exist. In particular, it is worth investigating the interaction between multi-wall CNTs and different type of polymer or epoxy matrix, and the influence over their mechanical and electrical properties.

In this chapter, dc transport measurements and voltage noise analysis on different polymer/carbon nanotubes composites are presented. The transport property measurements show that a random tunnel junctions resistive networks model well describes all the compounds under test. In particular, with increasing the temperature, a crossover from a two-level tunneling mechanism to resistance fluctuations percolative paths induced has also been observed. Moreover, this *1/f* noise trend seems to be a general feature of the investigated highly conductive samples, going beyond the type of polymer matrix and nanotubes concentration.

3.1 Materials and methods

The investigated composites were prepared by mixing CNTs in different polymeric matrices. MWCNTs were synthesized by chemical vapor deposition at CSIRO (Commonwealth Scientific and Industrial Research Organization, Australia) and dispersed in two polyethylene bases, with an average molecular weight of

≈60000 g/mol and a polydispersity of 5.8 (High-density polyethylene HDPE0390 from Qenos) and ≈115000 g/mol and a polydispersity of 7.6 (Low-density polyethylene LDPE from Scientific Polymer Products), respectively, with two MWCNT concentrations (5 and 7 wt%). In addition, MWCNTs synthesized by catalytic carbon vapor deposition process (Nanocyl S.A.) were incorporated in a diglycidil-ether bisphenol-A (DGEBA) epoxy resin, with a concentration of 0.5 wt%. Basically, polymeric matrix compound is considered as insulating material because of its high electrical resistivity (10^{10}-10^{15} Ωm). Injecting conductive material into the insulating matrix can lead to an overall conductive compound, strongly depending on the volume fraction of the conductive phase. In particular, below a threshold volume fraction, the conductibility of the composite dramatically increases by several orders of magnitude due to percolation. In conclusion, CNTs add several features to the composites: at low loading, CNTs act as a conductive additive, due to their low percolation thresholds (between 1 and 2.5 wt% for HDPE and LDPE, and lower than 0.1 wt% for epoxy), while uniformly dispersed in higher percentage, enhance its mechanical properties [9]. The detailed information reported in [10] and [11] indicate that all the used polymer/carbon nanotubes compounds are suitable for sensor and conductor applications, due to their high conductivity values. This behavior of the composites seems to be not influenced by the presence of a bundle organization which, however, has been observed through a scanning electron microscopy analysis.

The experimental setup provides both two- and four-probe connections to the samples through evaporated gold contact pads (25-nm-thick, 5-mm-wide and about 1-mm-distant). All the measurement were carried out by using the experimental setup described in the chapter 1. Possible effects of spurious external noise sources were eliminated by resorting to proper techniques, as described in [12].

3.2 DC electrical transport properties

The temperature dependence of the resistance *R* for the five investigated MWCNT composites is shown in Fig. 3.1. The clear monotonic decrease with increasing temperature is best interpreted by Sheng model [13]. Other possible models, such as variable range hopping and Luttinger liquid models reproduce the experimental data, but does not give a low reduced χ^2 and the high coefficient of determination values compared to Sheng model.

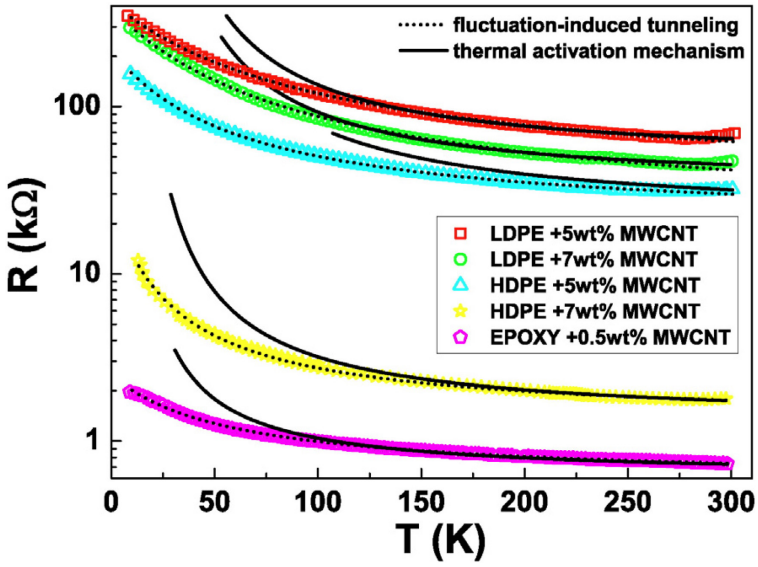

Figure 3.1 Temperature dependence of the resistance *R* for the five different types of investigated MWCNT compounds. The dashed and solid lines are the best fitting curves with Eqs. (3.1) and (3.2)

In the case of carbon nanotubes compounds [14], a fluctuation-induced tunneling conduction between conducting regions (the MWCNTs) and small insulating barriers (the matrix) is modeled through the following expression

$$R(T) = R_0 \, exp\left(\frac{T_1}{T + T_0}\right) \tag{3.1}$$

where R_0 is a preexponential factor, and T_0 and T_1 are two characteristic temperatures of the systems under test [13]. The best fit curves by using Eq. (3.1) are shown in Fig. 3.1 as dashed lines, revealing a good agreement with the data points along the whole temperature range and for all the samples. The estimation of T_1, reported in Table 3.1 together with all the other fitting parameters, allows the evaluation of the minimum energy ($\Delta\epsilon_b \simeq k_B T_1$) necessary to cross the insulating barriers formed among the nanotube aggregates [14]. These values in Table 3.1 are similar to those observed for various carbonaceous materials, analyzed in terms of the Sheng model.

composite	R_0 ($k\Omega$)	R_1 ($k\Omega$)	T_0 (K)	T_1 (K)	$\Delta\epsilon_b$ (meV)	T_c (K)	ϵ_A
LDPE +5 wt%	31.2±0.4	51.4±0.9	106±1	278±4	23.9±0.3	137±4	0.334±0.007
LDPE +7 wt%	20.1±0.4	36.3±0.8	98±1	290±4	24.9±0.3	109±3	0.351±0.007
HDPE +5 wt%	19.5±0.4	19.8±0.5	65.0±0.8	157±2	13.5±0.2	>300	0.281±0.006
HDPE +7 wt%	1.31±0.03	1.29±0.03	32.2±0.5	97±1	8.3±0.1	177±5	0.304±0.006
epoxy +0.5 wt%	0.58±0.01	0.64±0.01	59.1±0.7	86±1	7.4±0.1	100±3	0.263±0.005

Table 3.1 Temperature dependence of the resistance *R* for the five different types of investigated MWCNT compounds. The dashed and solid lines are the best fitting curves with Eqs. (3.1) and (3.2)

In the high-temperature region, a different conduction mechanism takes place due to the thermal activation over the potential barrier [15].The temperature dependence of the resistance is described by

$$R(T) = R_1 \, exp\left[\frac{T_c T_1}{T(T_c + T_0)} (1 - \epsilon_A)^2 \right] \tag{3.2}$$

Where R_1 is a preexponential factor, ϵ_A is the dimensionless applied electric field, and T_c is a crossover temperature above which the fluctuation-induced tunneling and thermal activation contributions are indistinguishable [13]. The solid lines shown in Fig. 3.1 are the best fitting curves with Eq. (3.2), and obtained with the values of T_c reported in Table 3.1. These crossover temperatures, associated to the energy distribution of the tunnel barriers, give an immediate morphological information on the interaction between the polymer matrix and the carbonaceous filler. It is worth to note that, in Eq. (3.2) the dimensionless applied electric field ϵ_A only gives, as a first approximation, a negligible contribution to the evaluation performed. However, the dc analysis, alone, is not able to identify the different transport mechanisms of charge carriers at high temperatures. In this context, noise spectroscopy is the right tool for a deeper insight.

3.3 Noise spectral density measurements

The spectral density of voltage fluctuations S_V is the physical quantity to examine if we want to deal with electric noise. The frequency dependence of S_V is shown in Fig. (3.2) for the different types of MWCNT compounds at the reference temperature of 300 K. All the spectra can be regarded as superposition of two main components: the first determines a *1/f* dependence in the low-frequency region and the second, characterized by a constant spectrum at higher frequencies, is due to the Johnson noise $4k_BTR$ added to the background electronic chain noise ($S_V \approx 1\times10^{-17}$ V^2/Hz).

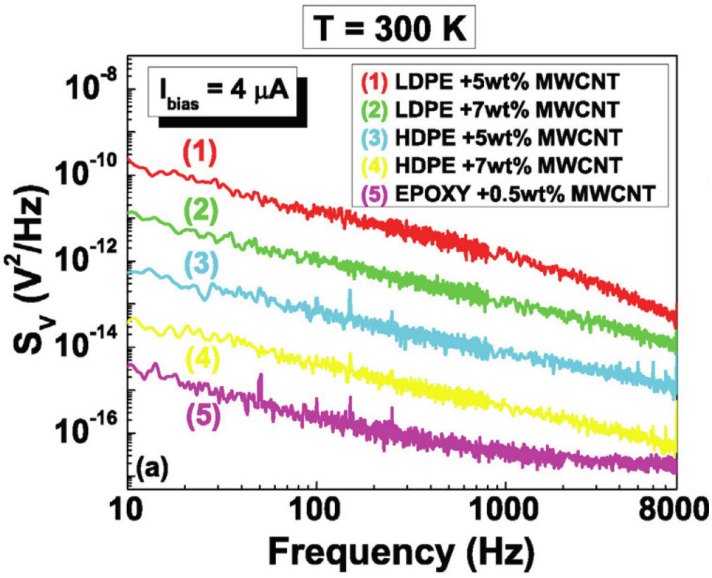

Figure 3.2 Spectral traces of all the investigated MWCNT composites at a reference temperature of 300 K and bias current of 4 μA.

In order to find out the dynamics of fluctuations and the conduction mechanisms, it is useful to study the *1/f* contribution versus the applied bias current. This dependence is shown in Fig. 3.3, revealing a quadratic behavior for all the samples under test and, as a consequence, resistance fluctuations as the dominant noise source.

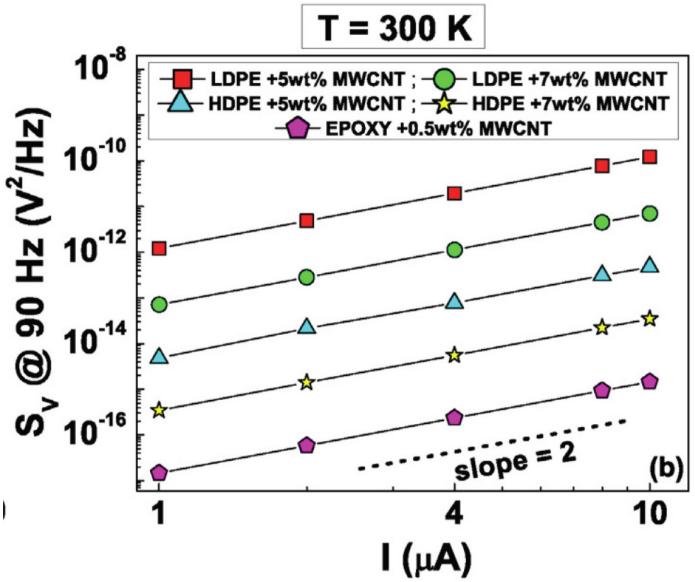

Figure 3.3 Quadratic bias dependence of the voltage-spectral density for all the investigated MWCNT composites at 90 Hz and at a reference temperature of 300 K.

In this framework, the noise level of Ohmic compounds can be expressed by using the Hooge relationship as [1]

$$Noise\,Level = \frac{f\,S_V}{R^2 I^2} = \frac{\alpha_H}{n}\frac{1}{\Omega_s} \tag{3.3}$$

where α_H is the dimensionless Hooge material-dependent constant, n the carrier density, and Ω_s the sample volume.

3.4 Fluctuation induced tunneling model applied to noise processes

The best way [15],[16],[17] to model the noise level in this kind of disordered systems is given by

$$Noise\,Level = \begin{cases} A\,T\,R^{-2} & T < T_c \\ S_0\,R^{w} & T > T_c \end{cases} \tag{3.4}$$

where A is a proportionality factor, S_0 is the amplitude of resistance fluctuations, w represents the critical indexes for lattice percolation, and T_c is the crossover temperature between the fluctuation-induced tunneling and thermal activation regimes. The parameters A and S_0, alone, are not sufficient to extract the intrinsic noise of the material, which is further dependent on the sample temperature, resistance, and volume. In details, below T_c, two-level tunneling system (TLTS) fluctuations dominate, while above T_c thermal activation must be considered, as a consequence of the percolation model [16]. It must be stressed that the two-level tunneling mechanism has successfully been used for the interpretation of the noise in individual nanotube samples [18], and also for HDPE compounds below the crossover temperature [7]. The experimental noise level, compared with the theoretical formulation given by Eq. (3.4), is shown in Fig. 3.4.

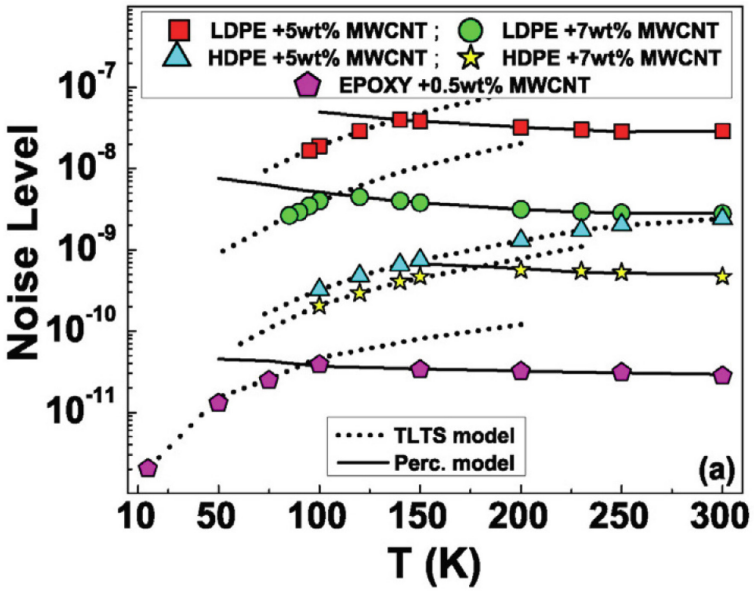

Figure 3.4 Temperature dependence of the Noise Level of all the investigated samples. The best fitting curves obtained by using a two-level tunneling system model [see Eq. (3.4), $T<T_c$] and a percolative noise mechanism [see Eq. (3.4), $T>T_c$] are shown as dashed and solid lines, respectively. The transition between these two regimes occurs at the crossover temperature, estimated from the dc analysis. The percolative model of HDPE +5wt% MWCNT composite is not shown, being out from the examined temperature range (T_c> 300 K).

Below T_c, the good agreement of TLTS model (dashed lines) with the data points is clear. On the other hand, the percolative fluctuation process (solid lines) prevails in the temperature region above T_c. Such a behavior is independent of the polymer matrix chosen for the device fabrication. By comparing Eq. (3.4) with Eq. (3.3), it is possible to extract the normalized Hooge parameter as

$$\frac{\alpha_H}{n} = \begin{cases} A\Omega_S T R^{-2} & T < T_c \\ S_0 \Omega_S R^w & T > T_c \end{cases} \qquad (3.5)$$

More in details, the exponent w assumes values of 1 for epoxy, 1.01 for LDPE, and 1.06 for HDPE. These are very close to the value predicted by the classical percolation theory in the case of three-dimensional systems [19]

The quantity α_H/n is evaluated by means of the Eq. (3.5), where Ω_s is the volume of the entire composite, that is the polymeric matrix and the conductive nanotubes. The results are shown in Fig. 3.5.

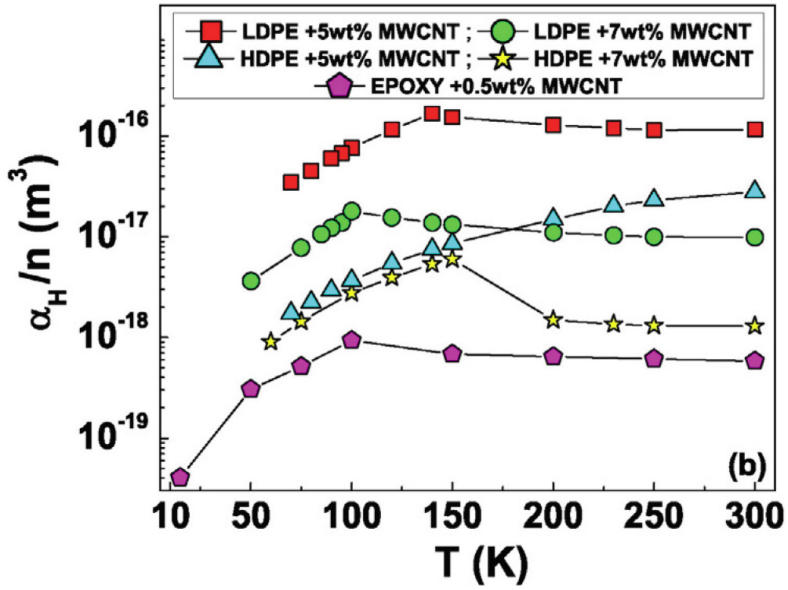

Figure 3.5 Temperature dependence of the normalized Hooge parameters computed with Eq. (3.5).

The epoxy based composite seems to be the most promising in high sensitivity applications, due to its lowest noise level in the whole investigated temperature range.

Author contribution The author performed the *R(T)* and voltage noise-measurements of all compounds. The author contributed to the theoretical interpretation of the experimental findings.

CHAPTER 4
Noise properties and transport in crystalline silicon-based solar cells

Crystalline silicon photovoltaic (PV) cells are the most common solar cells used in commercially available solar panels, representing more than 90% of world PV cell market sales in 2012. Crystalline silicon PV cells have laboratory energy conversion efficiencies over 25% for single-crystal cells and over 20% for multicrystalline cells. However, industrially produced solar modules currently achieve efficiencies around 20% under standard test conditions.

It is well known that quality and efficiency of Crystalline silicon PV cells are related to several electronic parameters of the defect states.

This chapter shows that low-frequency noise spectroscopy is a powerful and unconventional tool for the investigation of the properties of the defect states in silicon-based solar cells. Around 1970, Van der Ziel [20] and Hsu [21] related the *1/f*-type noise in the metal-oxide-semiconductor system and in p-n junctions to the fluctuation of the defect state population. Twenty years later, Jones [22] and Chobola [23] proposed low-frequency electric noise analysis to estimate quality of solar cells. Semiconductors often exhibit a *1/f*-type noise spectrum. Semi-empirical models have been formulated to correlate the current noise to mobility fluctuations [24], to the number fluctuation of free charge carriers within the space charge region [25], or to the semiconductor surface.

A theoretical model, combining trapping/detrapping and recombination mechanisms, is formulated to shed light on the origin of random current fluctuations in silicon-based solar cells. The comparison between dark and photo-induced noise allows the determination of important electronic parameters of the defect states. A detailed analysis of the electric noise, in several conditions of temperatures and for different illumination levels, is reported for crystalline silicon-based solar cells, in the pristine form and after artificial degradation with high energy protons. The evolution of the dominating defect properties is studied through noise spectroscopy.

Findings suggest that the formation of the defects, activated under illumination or charge carrier injection, is related to long-term degradation of the solar cells. Moreover, noise analysis provides interesting information on radiation damage, and can be used for a detailed temperature-dependent electrical characterization of the charge carrier capture/emission and recombination kinetics. This aspect represents an advantage of the fluctuation spectroscopic technique, which gives the possibility to directly evaluate the cell health state.

4.1 Materials and methods

The investigated solar cells, type "SC2140-Z8-24" were manufactured by SOLARTEC (Radhoštěm, Czech Republic). The useful area A of the photovoltaic devices was 1 cm^2 with a wafer thickness d of 320 μm. The starting efficiency of pristine samples was 15% under AM 1.5 G conditions, with a short-circuit current I_{sc} = 37.45 mA, open-circuit voltage V_{oc} = 581 mV, and fill factor FF = 68.96%. Degradation effects were artificially induced on the devices with proton irradiation at the Helmholtz-Zentrum Berlin für Materialien und Energie (Germany), with a proton energy of 65 MeV in air. A homogeneous defect distribution, with this energy value, was verified by using a SRIM (Stopping and Range of Ions in Matter) code. Additional details on the performed analysis can be found in [26]. The samples were irradiated with three different proton fluences: 2×10^{11} protons/cm^2, 1×10^{12} protons/cm^2, and 5×10^{12} protons/cm^2. All the measurements were carried out by varying the temperature from 280 to 340 K with a thermoelectric cooler, and by stabilizing it with a computer-controlled PID loop to better than 0.1 K. The cool white Light Emitting Diode (LED) "KLC8 Edixeon K series", from Edison Opto, was used as light source. The choice of the LED as light source ensured a low-noise source, allowing to discriminate intrinsic photo-induced mechanisms from extrinsic ones, potentially related to the complex electronics of the solar simulator. The setup for the electrical transport and noise characterizations was arranged in order to minimize the presence of spurious components in the measured spectral traces. External noise contributions, such as light source emission noise, light source bias circuit noise were also evaluated and found to be negligible as reported in the Supplementary information of [27].

4.2 Noise model of solar cells

Bias voltage, photogeneration processes and diode geometry greatly affect fluctuations phenomena in p-n junctions. When defect states are present, the trapping and recombination mechanism of the charge carriers gives rise to current fluctuations, which represent the main noise source [28]. The amplitude of the random current fluctuations *Var [I]* is, therefore, related to the occupation probability f_{trap} of the traps. The recombination pathways from the conduction band to the valence band generate a decrease of the minority charge carriers stored in the base material, and this effect also influences *Var [I]*. The contribution of the traps can be modeled by the means of two energy levels, which act as trapping (E_T) and recombination (E_{SRH}) centers. These centers, located above the intrinsic Fermi level E_i (see Fig. 4.1 (a)) are responsible for the transitions between the defect states and the conduction E_C and valence E_V bands. Under photogenerated or injected charge carriers, the E_T energetic states

are able to capture and emit electrons from the conduction band and the E_{SRH} states work as Shockley-Read-Hall (SRH) type recombination centers with an associated lifetime τ_{SRH} [29].

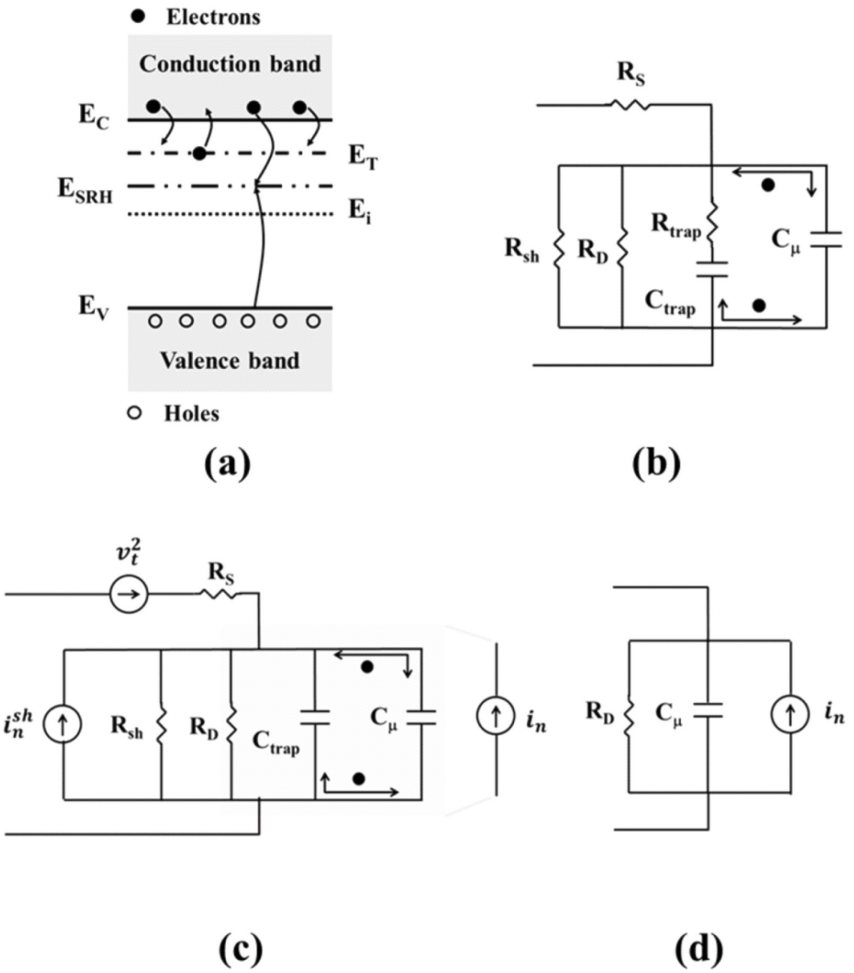

Figure 4.1 (a) Energy-band diagram of the silicon showing carrier recombination and trapping processes. **(b)** ac electrical equivalent circuit of the solar cell. **(c)** Equivalent circuit including noise sources. **(d)** Simplified version.

The fluctuating traps with energy level E_T can be modeled by a series *RC* circuit in parallel to C_μ [30], as shown in Fig. 4.1 (b) where the differential resistance R_D and the capacitance C_μ represent the contribution of the minority charge carriers into the base material. Moreover the cell shunt R_{sh} and series R_S resistances take into account the recombination loss and ohmic series resistance respectively. Usually $R_{sh} \gg R_D$ and the recombination phenomena, associated to the defect states, can be well described by the time constant $\tau_{eff} = R_D C_\mu$. The density of empty traps into the base material can be modeled by a capacitance contribution C_{trap}, which is related to the variation of f_{trap} with respect to the

quasi-Fermi level under nonequilibrium condition (charge carrier injection). On the other hand, the resistance R_{trap} represents the kinetic factor of the traps [30], which characteristic trapping/detrapping time is $\tau_{trap} = R_{trap} C_{trap}$. Below the frequency $(2\pi\tau_{trap})^{-1}$, the capacitive contribution of the fluctuating trap states is important so that noise spectroscopy is able to follow the charge carrier transfer from the conduction band to empty traps and viceversa (see Fig. 4.1 (c)). This mechanism leads to fluctuations in the number of charge carriers and contributes, therefore, to a current fluctuation that can be measured by the external contacts. The effect of these traps can be modeled as a current-noise source in, which represents the charge carriers transfer between C_{trap} and C_{μ} (see Fig. 4.1 (d)). The solar cell equivalent noise circuit can be assumed as simply composed by the parallel connection of C_{μ}, R_D, and i_n, as shown in Fig. 4.1 (d). The noise is generated by the variation in the number of carriers, that are typically present in the cell, due to the dc bias or light absorption. A characteristic *1/f* frequency spectrum is observed, with the presence of a cut-off frequency given by $f_x = (2\pi\tau_{eff})^{-1}$ [31].

In this context, the amplitude *Var [I]* of the *1/f* noise component can be defined as the sum of a dark (*Var [I_{dark}]*) and a photo-induced (*Var [I_{ph}]*) contribution. Under dark condition and on forward biasing of the solar cell, the *Var [I_{dark}]* value is influenced by the emission rates $e_{n,p}$ and volumetric capture coefficients per unit time $c_{n,p}$ for the electron and hole traps [29]. When the cell is illuminated, these capture coefficients, the emission rates and the density of filled traps change. Consequently, the process of carrier photogeneration increases the trap filling up to a saturation point, meaning that all traps have been activated from the noise point of view. In this condition, the *Var [I_{ph}]* contribution is dominant, being larger than the dark background noise. The photogenerated current can be expressed as [32]

$$I_{ph} = \frac{q}{\tau_{eff}} A d n \tag{4.1}$$

where q is the elementary charge, n is the average excess carrier density, and A and d are the sample area and thickness, respectively. By taking SRH statistics into account, the fraction n_T of the filled fluctuating traps is [32]

$$n_T = \frac{N_T e_n}{e_n + c_n n} \tag{4.2}$$

The fraction of the filled recombination centers is [32]

$$n_{SRH} = \frac{N_{SRH} c_p N_A}{c_n n + c_p N_A} \tag{4.3}$$

where N_A is the base doping concentration. In Eq. (4.1) it is worth noting that the only fluctuating term is related to *n*, therefore, under the assumption of a binomial probability distribution, *Var [I_{ph}]* can be expressed as [1]

$$Var\left[I_{ph} \right] = \left(\frac{q}{\tau_{eff}} \right)^2 \{ Var[Adn_T] + Var[Adn_{SRH}] \} \tag{4.4}$$

Substituting Eq. (4.2) and (4.3) into Eq. (4.4) follows

$$Var[I_{ph}] = \left(\frac{q}{\tau_{eff}} \right)^2 Ad \left[N_T \frac{n\frac{c_n}{e_n}}{\left(1 + n\frac{c_n}{e_n}\right)^2} + \frac{N_{SRH}}{N_A}\frac{c_n}{c_p}\frac{n}{\left(1 + \frac{n}{N_A}\frac{c_n}{c_p}\right)^2} \right] \tag{4.5}$$

where $c_n/c_p = k$ is the symmetric ratio [33].

Moreover

$$I_0^{light} = \frac{q}{\tau_{eff}} Ad \frac{e_n}{c_n} \tag{4.6}$$

and

$$I_A = \frac{q}{\tau_{eff}} Ad \frac{N_A}{k} \tag{4.7}$$

Eq. (4.5) can be rewritten as

$$Var\left[I_{ph} \right] = A_1 \frac{I_{ph}}{\left(1 + \frac{I_{ph}}{I_0^{light}}\right)^2} + A_2 \frac{I_{ph}}{\left(1 + \frac{I_{ph}}{I_A}\right)^2} \tag{4.8}$$

where

$$A_1 = \frac{q}{\tau_{eff}} N_T \frac{c_n}{e_n} \qquad \text{and} \qquad A_2 = \frac{q}{\tau_{eff}} N_{SRH} \frac{k}{N_A} \tag{4.9}$$

represent the amplitudes of the current fluctuations related to the trapping and recombination mechanisms, respectively. When the noise level is almost

saturated the threshold current I_0^{light} happens, and I_A takes into account the influence of the recombination centers.

4.3 Noise spectral density measurements

The effectiveness of the proposed noise model has been verified by measuring the same type of Si-based solar cells, in two different form: pristine and proton irradiated to gain an increasing numbers of traps.

Pristine Si-based solar cells. The first step is the acquisition of the voltage-spectral density S_V generated by the device in various operation conditions. In Fig. 4.2, the Voltage-spectral density of pristine solar cells is shown at a temperature of 300 K and for different bias points, corresponding to several differential resistance values. A large *1/f* component is evident, followed by a constant amplitude spectrum at higher frequencies, both in dark, see Fig. 4.2 (a), and under illumination, see Fig. 4.2 (b). The measured noise can be expressed as [1]

$$S_V = \frac{K}{f^{\gamma}} + \mathrm{C} \tag{4.10}$$

Where K is the voltage-noise amplitude, γ = (1.18 ± 0.02) is the frequency exponent, and C = 1.04 × 10^{-17} V^2/Hz is a negligible frequency-independent noise component, due to the readout electronics.

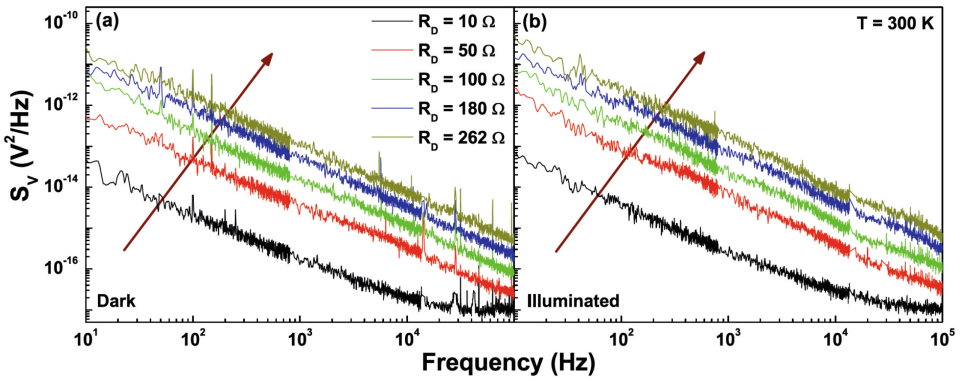

Figure 4.2 (a) Frequency dependence of S_v at 300 K and for increasing values of the differential resistance R_D in dark condition. **(b)** Frequency dependence of S_v at 300 K and for increasing values of the differential resistance R_D under illumination.

After a careful examination of the *1/f* noise, interesting information on the conduction mechanisms and the dynamics of fluctuations can be extracted. The variance of the voltage is given by [1]

$$Var[V] = \int_{f_{\min}}^{f_{\max}} df\, S_V = K \frac{f_{\max}^{(1-\gamma)} - f_{\min}^{(1-\gamma)}}{(1-\gamma)} \tag{4.11}$$

where the frequency interval [f_{min}, f_{max}] = [1, 100000] Hz is the experimental bandwidth, and γ ≠ 1. The *Var* [*V*] exhibits a quadratic dependence on R_D not depending on illumination and temperature conditions, as shown in Fig. 4.3 (a) for the sample temperature of 300 K.

This behavior indicates that current fluctuations are the dominant noise source in the photovoltaic system. The amplitude is given by [1]

$$Var[I] = \frac{Var[V]}{R_D^2} \tag{4.12}$$

and is independent on RD, as clearly evident in Fig. 4.3 (b).

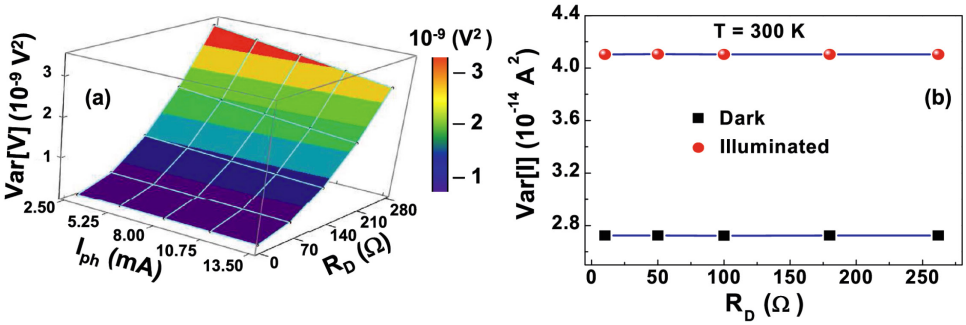

Figure 4.3 (a) Dependence of the *1/f* voltage noise amplitude on the differential resistance and on photocurrent at 300 K. **(b)** Dependence of the current fluctuations amplitude on the differential resistance under illumination at 18 mW/cm^2 (circles) and under dark condition (squares) at 300 K.

The photo-induced fluctuations amplitude has been analyzed at a fixed bias condition of R_D = 10 Ω, and is shown as current noise in Fig. 4.4 at four different temperatures ranging from 280 to 340 K.

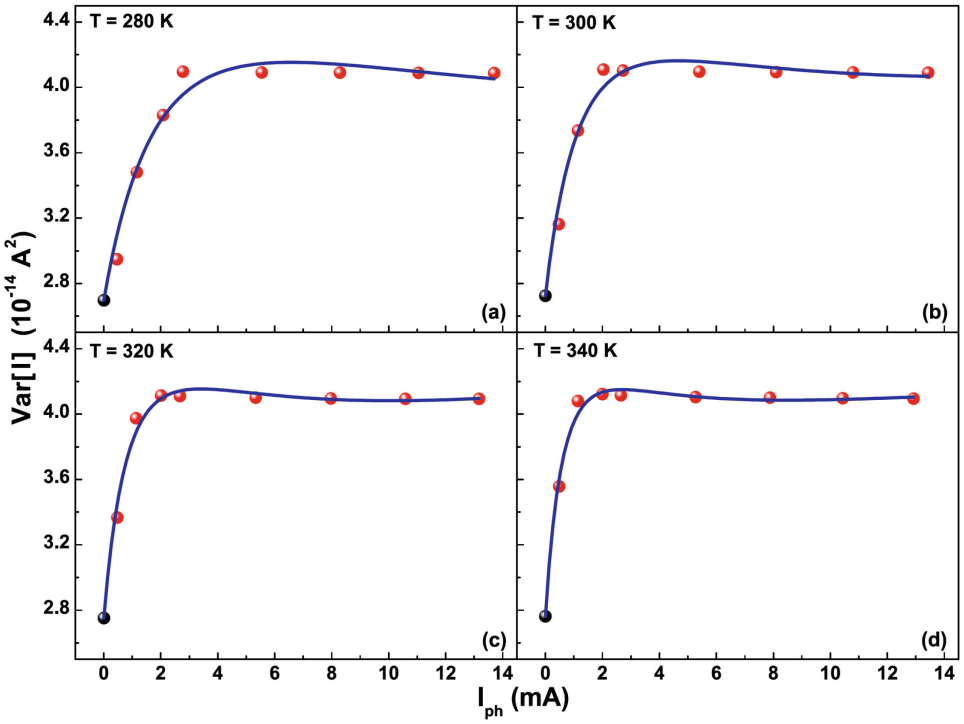

Figure 4.4 Photocurrent dependence of the current fluctuations amplitude at 280 K **(a)** , 300 K **(b)** , 320 K **(c)** and 340 K **(d)**. The blue solid lines represent the best fitting curves using Eq. (4.8), while black dots represent noise level in dark condition.

Under the low-level injection operating conditions of most silicon solar cells [34], the SRH recombination is the dominant mechanism influencing the minority charge carrier lifetime. In this framework, it can be assumed that $\tau_{eff} = \tau_{SRH}$. Furthermore,

$$\tau_{SRH} = \tau_{n0}\left(1+\frac{I_0^{light}}{I_A}\right) \tag{4.13}$$

where $\tau_{n0}=(c_n N_{SRH})^{-1}$ and $I_0^{light} / I_A \ll 1$. It follows that $\tau_{SRH} \approx \tau_{n0}$ but τ_{n0} is weakly temperature-dependent below 340 K [33], so the value of τ_{eff} can be assumed constant [26]. It is worth noting that the effective lifetime can be directly estimated from the noise spectra, when the cut-off frequency occurs within the experimental frequency bandwidth [31]. By using Eq. (4.6), Eq. (4.7) and Eq. (4.9) it is possible to compute the most important defect states parameters including the number of the fluctuating traps N_T .

The temperature dependence of N_T is reported in Fig. 4.5 (left axis), and it does not change within the experimental errors in the whole analyzed temperature range.

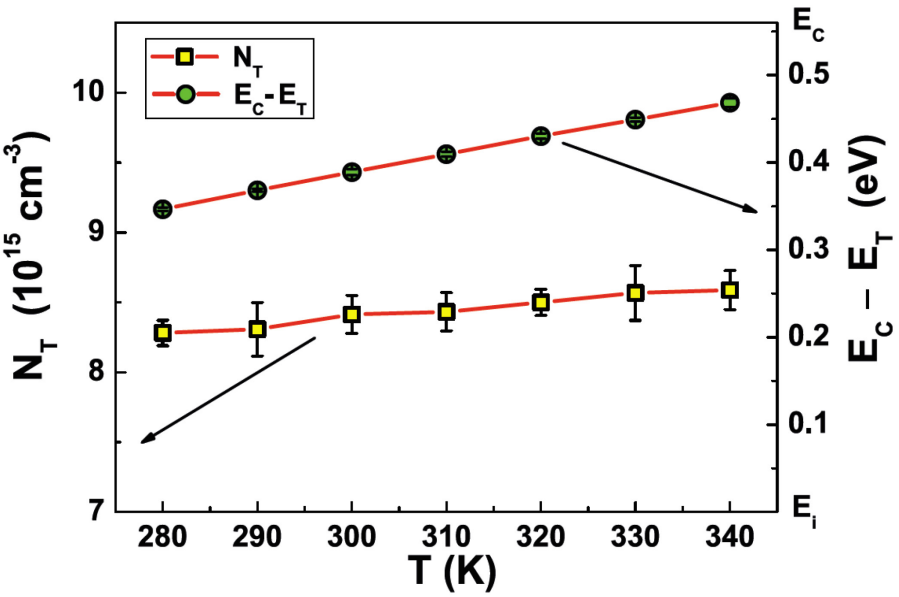

Figure 4.5 The fluctuating trap density N_T is shown as a function of temperature on the left y-axis (yellow squares), while the energy depth of the traps $E_C - E_T$ is shown on the right y-axis (green circles). For a better readability, the right scale only reports the upper half $E_C - E_i$ of the bandgap.

It must be stressed that, the average value of N_T = (8.4 ± 0.1) × 10^{15} cm^{-3} is close to the doping concentration N_A ≈ 9 × 10^{15} cm^{-3}, and this is consistent with the formation of unstable boron-oxygen defects. A further validation comes from the energy depth of the traps below the conduction band, that can be estimated from

$$E_C - E_T = k_B T \ln\left(\frac{N_c}{I_0^{light}}\frac{q}{\tau_{eff}}Ad\right) \tag{4.14}$$

where k_B is the Boltzmann constant, T the temperature, and N_C the effective density of states in the conduction band [32]. The temperature dependence of the trap energy is shown in Fig. 4.5 (right axis), from which an average value of E_C–E_T = (0.41 ± 0.04) eV can be evaluated. Once again, the estimations of E_C–E_T and of the symmetric ratio k = (30.9 ± 0.8) at 300 K are consistent for a metastable boron-oxygen defect in Czochralski grown silicon, as reported in literature where k = 6.2 − 33.6 and $E_C - E_T$ = 0.39 − 0.46 eV [33].

Proton irradiated Si-based solar cells. The frequency dependence of S_V found for pristine devices is also observed for all the silicon solar cells irradiated with different proton fluences. In Fig. 4.6 (a), the presence of a *1/f* noise component followed by a constant amplitude spectrum at higher frequencies is clear. The current-noise amplitude *Var* [*I*] can be computed from Eq. (4.12) and does not depend on R_D, (see Fig. 4.6 (b)) due to the fact that the *1/f* contribution is characterized by a quadratic dependence on the differential resistance R_D. Again, the overall trend is completely independent on proton irradiation, light intensity and temperature, thus indicating current fluctuations as the dominant noise source [1].

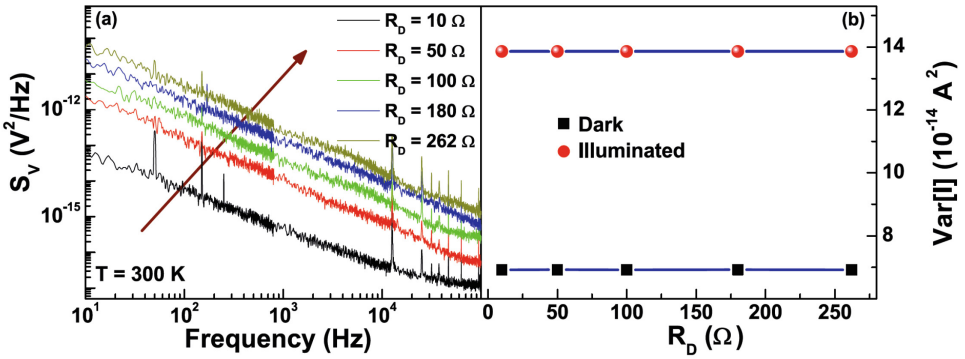

Figure 4.6 (a) Frequency dependence of S_v at 300 K and for increasing values of the differential resistance R_D for a proton irradiated silicon solar cell with fluence of 5 x 10^{12} protons/cm^2. **(b)** Frequency dependence of S_v at 300 K and for increasing values of the differential resistance R_D under illumination.

By comparing the photocurrent dependence with that of pristine devices it is found to be similar. Therefore the theoretical model of Eq. (4.8) can be applied to the artificially degraded silicon solar cells too. The results are depicted in Fig. 4.7.

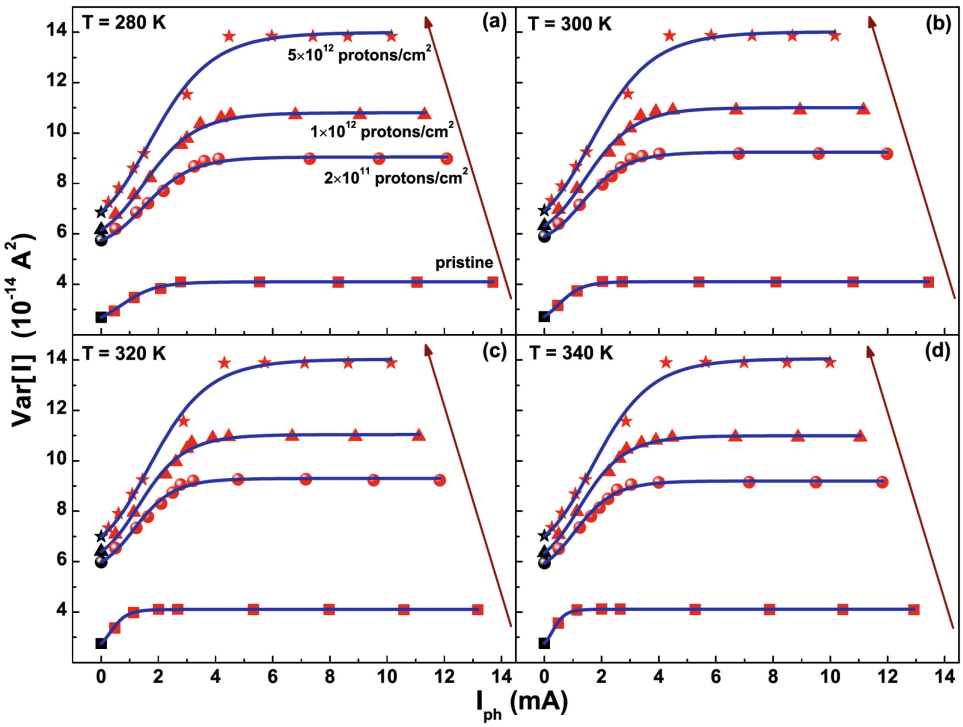

Figure 4.7 Dependence of the current fluctuations amplitude on the photocurrent for pristine and irradiated devices and for temperature ranging from 280 K to 320K. The experimental data points (red) and the best fitting curves (blue solid lines) descend from Eq. (4.8). The arrows show the increasing proton fluences.

The dependence on irradiation level of the defect states parameters, extracted from the noise analysis, allows to evaluate the effect of radiation exposure, and the corresponding damage of the cells, which is also associated to a decrease of the energy conversion efficiency [26]. In Fig. 4.8 (left axis), is shown the density N_T of active traps contributing significantly to the noise signal, that increases with the fluence of proton irradiation. This occurrence gives a direct indication of the presence of additional degradation processes in the photovoltaic device, confirmed by the increase of the dark background noise amplitude. It proves that the defects induced by damaging the samples have the same role in the fluctuation mechanisms both in dark and under illumination. At the same time, a weak decrease of the trap energy depth is displayed in Fig. 4.8 (right axis).

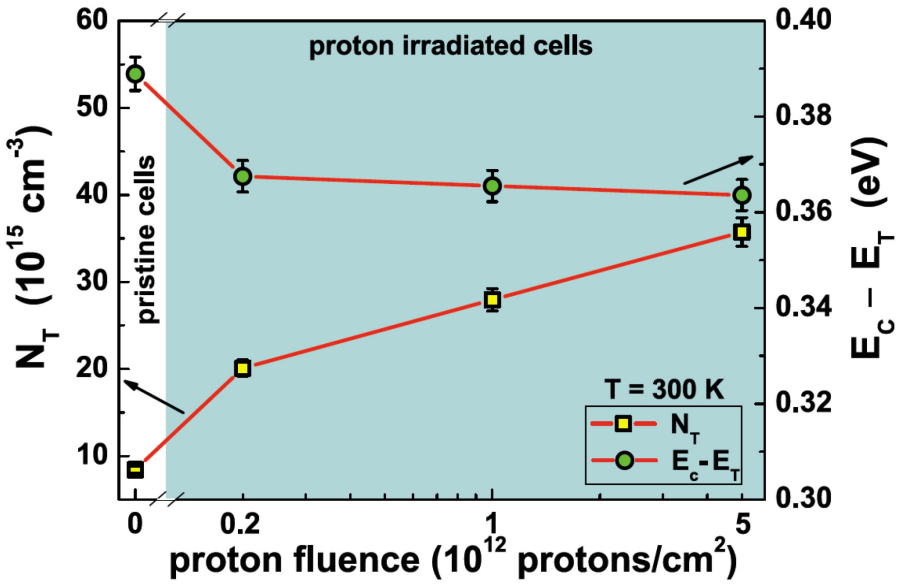

Figure 4.8 Proton fluence dependence of the fluctuating trap density N_T (left y-axis and yellow squares), and of the energy depth of the traps $E_C - E_T$ (right y-axis and green circles), at 300 K.

The observed effects on N_T and on E_C–E_T are consistent with the reported long wavelength decrease of the external quantum efficiency (EQE), due to the increase of recombination centers density caused by proton irradiation [26]. Moreover, in Fig. 4.8, it is worth noting the abrupt change after the first dose of radiation. This finding suggests that the major disturbance of the structure, leading to a noise enhancement, occurs at the beginning of radiation exposure. The values reported in Table 4.1 support this experimental evidence. In particular, the simultaneous decrease of the main solar cell photoelectric parameters and the increase of trap density seem to be directly related to an overall reduction in the power conversion efficiency (PCE).

Fluence (p^+/cm^2)	$V_{oc}\,(mV)$	$I_{sc}\,(mA)$	$\eta\,(\%)$	$N_T\,(10^{15}\,cm^{-3})$
0	(581 ± 6)	(37.4 ± 0.5)	(15.0 ± 0.3)	(8.4 ± 0.4)
2×10^{11}	(567 ± 5)	(34.2 ± 0.4)	(14.1 ± 0.3)	(20.1 ± 0.9)
1×10^{12}	(547 ± 5)	(31.7 ± 0.4)	(12.7 ± 0.2)	(28 ± 1)
5×10^{12}	(518 ± 4)	(27.3 ± 0.3)	(10.3 ± 0.2)	(36 ± 2)

Table 4.1 Main parameters, at room temperature, of the Si-based solar cell for the evaluation of the degradation induced by proton irradiation. Open-circuit voltage V_{oc}, short-circuit current I_{sc}, and power conversion efficiency η are extracted from dc analysis, while total trap density N_T is extracted from noise measurements.

In conclusion, it has been shown that the proposed theoretical model is able to explain the nature of current fluctuations in solar cells and it has been verified

both on pristine and artificially degraded Si-based devices. In particular, a combination of trapping/detrapping processes and charge carrier recombination phenomena has been considered to explain the current fluctuation mechanisms. In pristine cells, the energetic position and the symmetric ratio are in good agreement with the values obtained by using alternative techniques, and well consistent with the boron-oxygen complex defect. On the other hand, in degraded devices, the total trap density increases with the fluence of proton irradiation and seems to be directly related to a decrease of the power conversion efficiency. All these findings prove that noise spectroscopy is a reliable tool for the electrical temperature-dependent characterization of electronic defects in photovoltaic devices too.

Author contribution The author contributed to the voltage noise-measurements of all devices. The author contributed to the discussion of the results and the implications.

CHAPTER 5
Noise properties and transport in polymer:fullerene solar cells

Organic solar cells promise low cost, flexibility, light weight, transparency, and large-area manufacturing compatibility. However, low stability and power conversion efficiency, when compared to inorganic technologies, still represent a limiting factor for the applicability of organic solar cells. The use of different combinations of donor-acceptor materials based on low band gap polymers and fullerene derivatives leads to a value of efficiency for the organic single junction solar cell higher than 10%. Recently, the addition of Fe_3O_4 nanoparticles as dopant within the P3HT:PCBM, improves efficiency up to 11% [35], while for organic tandem devices, η exceeds 12% [36]. A balanced interaction between donor and acceptor materials is fundamental to ensure a high rate of charge carriers and to lower the recombination rate between electrons and holes in the blend. It is well known that the loss mechanisms are mainly related to recombination of the charge-separated excitons [37].

Film ordering strongly affects recombination and transport in the active layer, so that a precise tuning of the nanoscale morphology of the blend by nanostructuring is essential.

In literature, several studies report the influence of the preparation conditions, such as deposition temperature and solvent additives, on the active layer morphology [38],[39]. The charge carrier recombination dynamics is often found to be bimolecular and is described by Langevin's theory. In this case, the recombination rate is proportional to the sum of the electron and hole mobilities. It is worth to remember that the mobility-lifetime product μτ gives a direct measurement of the correlation between recombination and the extraction of charges. In order to compare the results from the noise analysis with the data reported in literature, the donor-acceptor materials in bulk heterojunction-type (BHJ) devices is a blend of poly(3-hexylthiophene) (P3HT) and [6,6]-phenyl-C61-butyric acid methyl ester (PCBM) which is the most common pair of P3HT:PCBM materials in BHJ devices and has been considered as a reference system. Here, voltage-noise analysis, together with structural and photoelectric measurements, have been performed in polymer:fullerene photovoltaic devices prepared with solvent additives. The experimental findings indicates that the use of solvent additives increases the mesoscopic order and crystallinity within the active layer, and induces a clear improvement of the charge carrier transport. The temperature dependence of the mobility and carrier lifetime suggests that in P3HT:PCBM blends the Langevin-type bimolecular recombination loss represents one of the major device limiting factors for the efficient extraction of the charge carriers.

5.1 Materials and methods

The active layers were fabricated using 1,2-dichlorobenzene (oDCB, boiling-point 180 °C) as the host solvent, and 1,2,3,4-tetrahydronaphthalene (THN, boiling-point 207 °C) as the additive (10% of the entire volume). Pure solutions of the host solvent oDCB were used to prepare the reference samples. P3HT (supplied from Merck Chemicals ltd) and PCBM (manufactured from Solenne BV) were dissolved in oDCB or in oDCB+THN in a 1:1 ratio in weight and stirred at 70 °C overnight before use [38]. The whole sample preparation took place in a nitrogen filled glovebox. Indium tin oxide (ITO) coated glass substrates (from PGO) were used as the anode. The substrates were patterned, cleaned in isopropyl alcohol, and exposed to an oxygen plasma. A layer of poly(3,4-ethylenedioxythiopene) (PEDOT):poly(styrenesulfonate) (PSS) (Clevios P VP Al 4083 from H.C. Starck) was then spun on top of the ITO and dried for 10 min at 180 °C. The active layer was spun on top of the PEDOT:PSS layer and annealed for 10 min at 150 °C. The film thicknesses were monitoredd using a Veeco Dektak 6M Profilmeter, resulting in values of 115 nm for oDCB and 130 nm for oDCB+THN. The thickness of the PEDOT:PSS layer was about 60 nm. The cathode was deposited by thermal evaporation of Ca and Al. The active area of the devices was 0.5 cm^2. The investigated device structure presents the following layer sequence, glass/ITO/PEDOT:PSS/P3HT:PCBM/Ca/Al and is shown in Fig. 5.1.

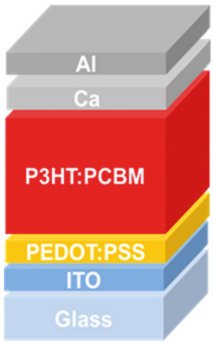

Figure 5.1 Sketch of the cross-section of the investigated polymer:fullerene solar cells.

Atomic force microscopy (AFM) analyses were performed in a UHV-STM/AFM from Omicron with a pressure below $5x10^{-10}$ mbar to avoid the effects of oxygen and humidity on the surface of the sample. Measurements were realized using a controller from Nanonis. Pt/Ir cantilevers from the company Nanosensors were calibrated before each measurement using a gold single crystal with 111-orientation as a reference [38].

To measure the J-V characteristics, the devices were illuminated with a KH Steuernagel solar sun simulator providing the standard reference spectrum AM1.5 G. A reference silicon solar cell provided by Fraunhofer ISE (Freiburg,

Germany) was used for the calibration. External quantum efficiency (EQE) was measured with a Xe–Hg tandem lamp using a two grating monochromator. A calibrated silicon photodector was used to monitor the incident photon flux. The photocurrent of the device was recorded using a lock-in amplifier. The temperature-dependent noise investigations were carried out by using a thermoelectric cooler Peltier-type device, with an operating range from 280 K to 340 K. A LM35 sensor in contact with the sample holder was used to measure the temperature, whose stabilization, better than 1 K, was realized through a computer-controlled feedback loop. The solar cells were biased with a low-noise Keithley dc current source. The output ac voltage signal was amplified with a low-noise Signal Recovery 5113 preamplifier and, subsequently, was analyzed with a dynamic signal analyzer HP35670A.

5.2 DC electrical transport properties

The solar cells prepared with 1,2-dichlorobenzene (oDCB) reference solvent and oDCB with 1,2,3,4-tetrahydronaphthalene (oDCB+THN) mixture solvent exhibit the current density-voltage (J-V) characteristics under illumination reported in Fig. 5.2 (a). By assuming the single diode model of the solar cell, the following parameters have been extracted for oDCB based devices: short circuit current density J_{SC} = (5.5 ± 0.3) mA cm^{-2}, open circuit voltage V_{OC} = (0.58 ± 0.03) V, fill factor *FF* = (69 ± 3)%, and a power conversion efficiency η = (2.2 ± 0.1)%. The same parameters for oDCB+THN are: J_{SC} = (7.4 ± 0.4) mA cm^{-2}, V_{OC} = (0.61 ± 0.03) V, *FF* = (72 ± 3)%, and η = (3.3 ± 0.2)%. The increase of the η value for the device fabricated with the solvent mixture is probably due to the increase of the J_{SC}. Variations in the *FF* and V_{OC} are within the experimental errors.

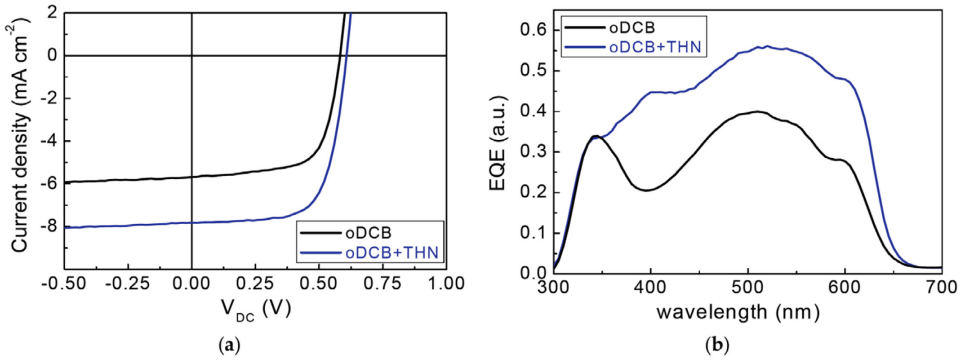

Figure 5.2 (a) Illuminated current density-voltage characteristics of solar cells with active layers prepared using the solvents oDCB (black line) and oDCB+THN (blue line). **(b)** The wavelength-dependent external (EQE) and internal quantum efficiency (IQE) plotted as black and red lines. The blue dashed line refers to the measured reflection *R* as (1 − *R*).

As can be observed, the oDCB+THN blend has a higher photocurrent, as compared to the blend prepared from pure oDCB. The external quantum efficiency (EQE) spectrum for both solar cells is shown in Fig. 6.2 (b). Following the J-V characteristics, the oDCB+THN blend shows a higher intensity of the EQE spectrum compared to the reference blend in the whole wavelength range. Here, the photocurrent density values evaluated from the integral of the EQE spectra are consistent with what estimated from the J-V characteristics: J_{SC} = 5.5 mA cm^{-2} for the oDCB solvent and 7.5 mA cm^{-2} for the oDCB+THN solvent.

Additionally, in the lowest EQE level, which depends on the oDCB blend, a marked drop in the spectrum between 350 and 450 nm is observed. This behavior has been already reported in literature for the P3HT:PCBM blend when a scarce ordering of the polymer is obtained during the film formation [40].

It is worth noting that the use of the tetralin leads to an increase of the crystalline order in the nanoscale crossing network for both the acceptor and donor components. The film ordering has a strong influence over the absorption spectra of the P3HT:PCBM layer, and the small rise located at 620 nm gives an indication of the P3HT crystallinity in the blend [38]. For the investigated samples, the relative intensity of the shoulder at 620 nm appears to be more pronounced in the blend deposited from oDCB+THN [8]. This suggests that the use of THN additive leads to a better phase segregation of the polymer and fullerene materials in the active blend. A further validation comes from the atomic force microscopy (AFM) analysis. Here, the average RMS roughness is ≈ 1.1 nm (oDCB blend) and ≈ 4.6 nm (oDCB+THN blend) [38] (see Fig. 5.3).

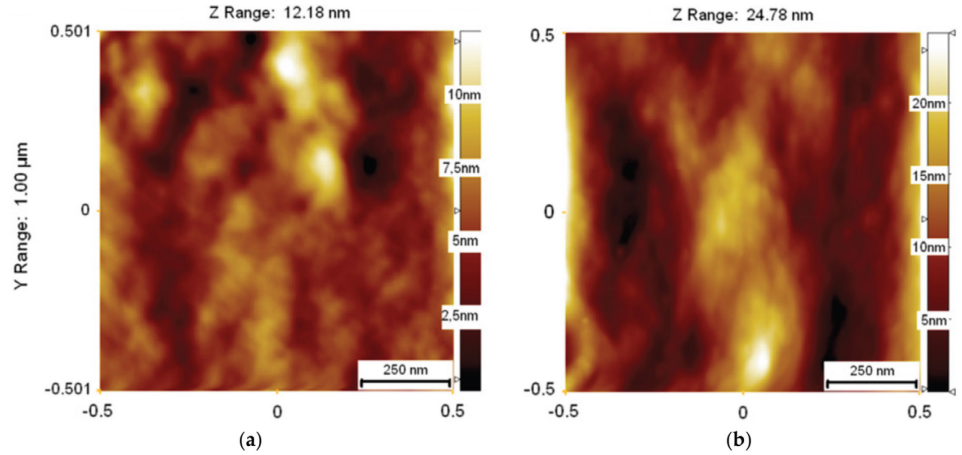

Figure 5.3 (a) Atomic force microscopy images of the blends prepared using the solvents oDCB. **(b)** Atomic force microscopy images of the blends prepared using the solvents oDCB+THN.

The ordering in the active layer of P3HT leads to improvements in the photocurrent and, consequently, also in the power conversion efficiency.

5.3 Noise spectral density measurements

The first step to gain information on the charge carrier fluctuation mechanisms is the measurement of the voltage-spectral density S_V generated by the device. It is reported both for the reference oDCB solvent (black spectra) and for the oDCB+THN (blue spectra) in Fig. 5.4, at a bias current I_{DC} of 20 μA and for two different temperatures of 300 K and 320 K in dark conditions.

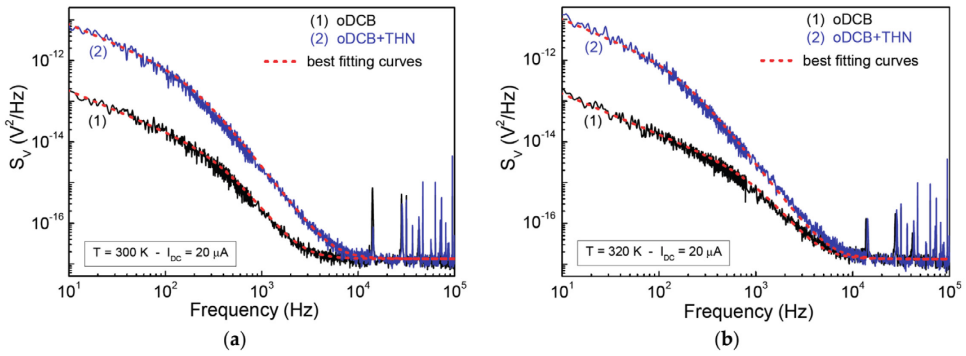

Figure 5.4 (a) Low-frequency voltage-noise spectra of a oDCB solvent based device, curves 1, and of a oDCB+THN solvent based device, curves 2 at 300 K. **(b)** Low-frequency voltage-noise spectra of a oDCB solvent based device, curves 1, and of a oDCB+THN solvent based device, curves 2 at 320 K.

Two distinct noise contributions can be identified. The first is the flicker noise $S_V^{flicker}$ dominating the low-frequency region and associated to electrical conductivity fluctuations [1]. The second one is the thermal noise $S_V^{thermal}$, which characterizes the high-frequency region of the spectrum and arises from temperature fluctuations of the charge carriers interacting with the polymeric chains [1]. The electronic behavior of the cells can be modeled by a simple RC circuit formed by the recombination resistance R_{rec} and the chemical capacitance C_μ of the active layer [41]. In this contest, it is possible to express S_V as [31]

$$S_V(f) = S_V^{flicker} + S_V^{thermal} = \frac{K}{f^\gamma}\frac{(R_{rec}I_{DC})^2}{1+\left(\frac{f}{f_x}\right)^2} + 4k_BTR_{rec} \qquad (5.1)$$

where K is the amplitude of the flicker noise component, γ is an exponent close to 1, f_x is a cut-off frequency at which a change from a $1/f$ to a $1/f^3$ dependence of the voltage-noise spectrum is observed, and k_B is the Boltzmann constant. The red dashed curves in Fig. 6.4 are the best fit obtained by using Eq. (5.1). The fitting parameters at 300 K are: K = (8.5±0.6)×10^{-11}, f_x = (199±6) Hz, and γ = (1.00±0.02) for the trace 1; while: K = (1.4±0.1)×10^{-9}, f_x = (133±4) Hz, and γ = (1.00±0.02) for the trace 2. From the best fitting values of the parameter

f_x can be extracted the time constant R_{rec} C_μ , useful to estimate the effective carrier lifetime as

$$\tau = (2\pi f_\chi)^{-1} = (2\pi R_{rec} C_\mu)^{-1} \quad (5.2)$$

The experimental values for τ are reported in Fig. 5.5 for temperatures ranging between 300 and 330 K and for the two types of solar cells investigated (oDCB solvent in pink region and oDCB+THN solvent in blue region).

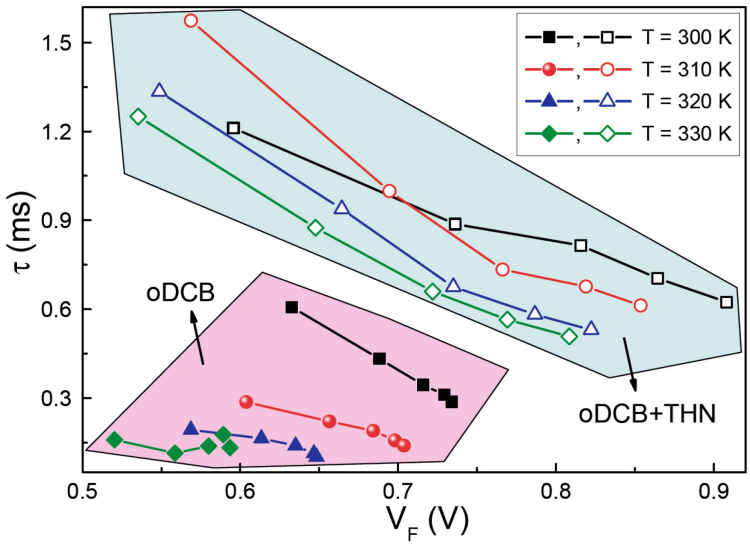

Figure 5.5 Effective carrier lifetime dependence on the forward voltage, at temperatures between 300 and 330 K. The experimental data are extracted by noise measurements. Full symbols refer to the oDCB solvent (pink region), while open symbols refer to the oDCB+THN solvent (blue region).

The adoption of the THN as solvent leads to an increase of τ. Indeed, at 300 K the observed effective lifetime ranges between 1.2 and 0.6 ms for the blend fabricated with the solvent mixture oDCB+THN. Conversely, the devices fabricated by using the reference solvent show lower values of τ, ranging between 0.8 and 0.2 ms. In addition, a decrease of τ while increasing the bias voltage, corresponding to an increase of the charge carriers stored within the organic device, has been found at all the investigated temperatures and for both types of solvents. This means that the recombination dynamics of the blend is bimolecular, since the effective lifetime τ depends on the charge carrier concentration n [42]. The lower values obtained for the device prepared with the reference solvent (full symbols in Fig. 5.5) indicate a strong recombination in the blend. On the opposite, higher values of τ, as observed for the THN based device (open symbols in Fig. 5.5), are indicative of a more efficient charge carrier transport in the active layer. It seems that the solvent mixture leads to a reduced charge carrier recombination rate, thus leading to an increase of the carrier

lifetime. This complies with the measurements on the electrical transport and the structural properties shown in Fig. 5.2 and Fig. 5.3. It is worth noting that for both the investigated devices, the carrier lifetime decreases with increasing temperature. This is a further proof that the dominant recombination losses within the device could be Langevin-type bimolecular recombination [43].

With the aim to ponder the role of the solvent on the film ordering in the blend and hence on the charge carrier transport, an evaluation of the carrier mobility has been made, starting from voltage-noise measurements.

The mobility can be computed from the amplitude of flicker and thermal noise components as [44]

$$\mu = \frac{k_B T}{e\tau E^2} \int_{f_{min}}^{f_{max}} \frac{s_V^{flicker}(f)}{s_V^{thermal}} df \tag{5.3}$$

being e the elementary charge, τ the carrier lifetime as defined in Eq. (5.2), $E = V_F/t$ the applied electric field (with t the active layer thickness), and $[f_{min}, f_{max}]$ the experimental frequency bandwidth. The resulting values from Eq. (5.3) are shown in Fig. 5.6.

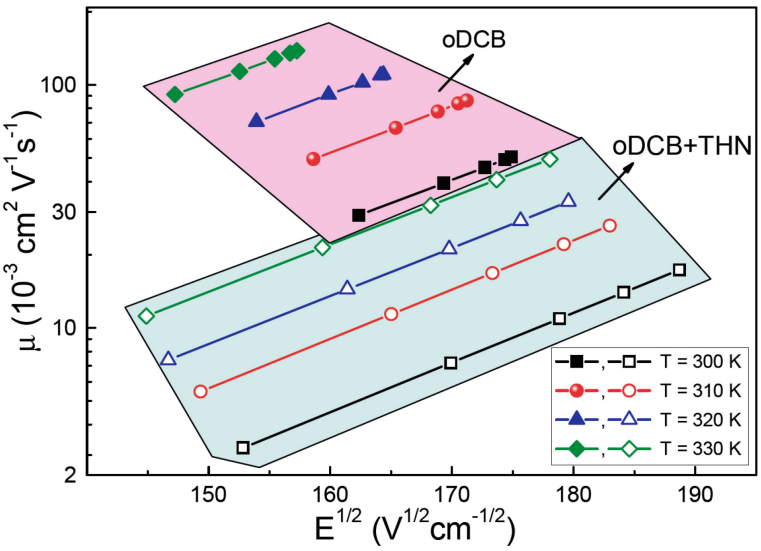

Figure 5.6 Electron mobility dependence, obtained by noise analysis, on the square root of the applied electric field. The best fitting curves (solid lines) are evaluated from the Poole-Frenkel model of Eq. (5.4), both for the oDCB solvent (full symbols) and the oDCB+THN solvent (open symbols).

A clear reduction of μ is evident for the cells with the oDCB+THN solvent (open symbols in blue region) upon respect to the reference solvent oDCB (full symbols in pink region) and for all the temperatures. Nevertheless, it is not possible to distinguish between electron and hole transport, but it is well-known that in P3HT:PCBM blends the electron mobility is higher than the hole mobility

[45]. As a consequence, the experimental data of Fig. 5.6 can be attributed to the electrons in the blends. The behaviour of μ with temperature and its bias dependence indicates that the dominant carrier transport mechanism is a thermally assisted hopping process between localized charge transport sites [43]. The exponential dependence of μ on $E^{1/2}$, visible in Fig. 5.6, can be interpreted in terms of the Poole-Frenkel model as [32]

$$\mu = \mu_0 \exp\left[\frac{e^{3/2}}{2k_B}\left(\frac{E}{\pi\epsilon_0\epsilon_r}\right)^{1/2}\frac{1}{T_{eff}}\right] \tag{5.4}$$

where ε_0 is the vacuum permittivity, $\varepsilon_r \approx 3$ is the relative dielectric constant for P3HT:PCBM, μ_0 is the zero-field mobility, and $T_{eff}^{-1} = T^{-1} - T_{Gill}^{-1}$ accounts for the Gill temperature at which the mobility is independent of the electric field. The best fitting curves, obtained from Eq. (5.4) with μ_0 and T_{eff} as free fitting parameters, are visible in Fig. 5.6 as solid lines.

The carrier transport within the blend move along nearest sites, located on the polymer and fullerene phases for the holes and electrons, respectively, by overcoming an energetic barrier. A precise estimation of the average value of the hopping barrier for the electrons can be performed by taking into account the Gill energy defined as $E_{Gill} = K_B T_{Gill}$ [46]. The temperature interactions of μ_0 and of E_{Gill} are reported in Fig. 6.7 and are connected to thermal activated processes within the active layer [46].

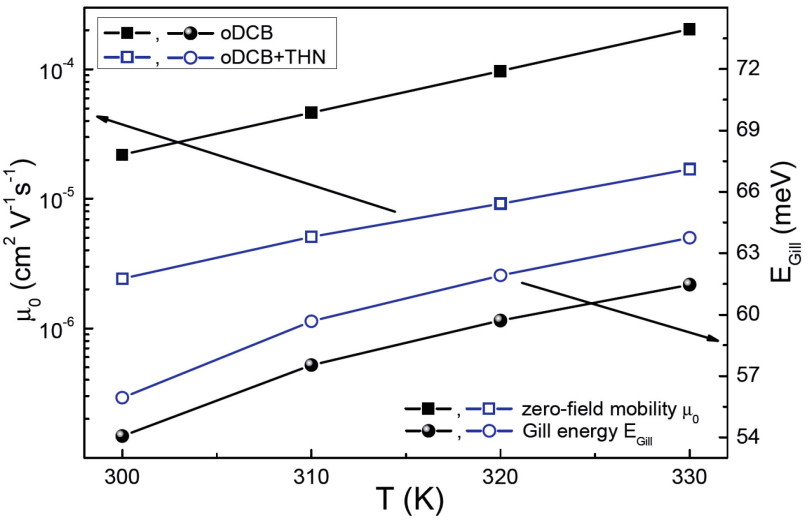

Figure 5.7 Temperature dependence of the zero-field mobility (left y-axis) and of the Gill energy (right y-axis). Full and open symbols correspond to oDCB and oDCB+THN solvent, respectively.

The use of the solvent mixture during the deposition phase produces a variation of E_{GiII} of less than 3%. The zero-field mobility (left y-axis in Fig. 5.7), extracted by noise measurements at 300 K of oDCB based devices, is μ_0 = (22±1)×10^{-6} cm2·V^{-1}·s^{-1} and is consistent with the value found in literature [38].

Conversely, the zero-field mobility for the device prepared by using oDCB+THN solvent is μ_0 =(2.4±0.1)×10^{-6} $cm^2V^{-1}s^{-1}$, lower than what found by using oDCB as solvent. This finding is consistent with the observed increased mesoscopic ordering in the blend. The increase of the film ordering induces a vertical phase separation between polymer and fullerene materials which causes a diffusion out of the PCBM material within the blend. The formation of a polymer rich phase reduces the charge carrier transfer so that also the zero-field electron mobility decreases for the blend prepared with the mixture solvent. However, it is interesting that the device prepared by using the oDCB+THN solvent exhibits a higher photocurrent value and, as a consequence, a higher conversion efficiency as compared to the solar cell fabricated with the reference solvent only. In polymer:fullerene solar cells, the photocurrent depends on to the light absorption in the active layer with the subsequent generation of excitons. The presence of THN influences the phase segregation within the blend with a scarce effect on the optical properties. It has already been verified that for the thicknesses of the blends investigated in this study (around 120 nm both for oDCB and for oDCB+THN) only a minimal difference in the short circuit current density is obtained [38]. Therefore, the difference in the J_{SC} values is essentially related to the recombination and transport mechanisms in the solar cell. The next step is to clarify the influence of the solvent on the charge carrier recombination process. The charge carrier recombination process in the bulk of semiconductor material is well explained by the Langevin theory. The recombination rate can be expressed as $R_L = \beta(np-n_i^2)$ with n and p electron and hole concentrations, respectively, and n_i the intrinsic carrier concentration. The Langevin recombination is given by

$$\beta = \frac{e}{\epsilon_r \epsilon_0}(\mu_n + \mu_h) \tag{5.5}$$

where e is the elementary charge, $\varepsilon_r\,\varepsilon_0$ the effective dielectric constant of the ambipolar semiconductor, and μ_n and μ_h are the electron and hole mobilities. By neglecting the recombination processes at the metal electrodes and by considering that the holes are solely transported in the donor polymer phase and electrons through the fullerene acceptor, a bimolecular recombination can only occurr at the heterojunction. Since $\mu_n >> \mu_h$, the higher carrier mobility values, at room temperature, are β = (17.6 ± 0.4)×10^{-9} cm^3s^{-1} and β=(4.3 ± 0.1)×10^{-9} cm^3s^{-1} for the oDCB and oDCB+THN solvent, respectively.

These values are in good agreement with typical recombination factors reported in literature for various organic solar cells. Again, the use of THN limits the recombination rate at the hetero-interface between the donor and the

acceptor phases, producing an increase of the carrier lifetime. Conversely, for the reference solvent a higher mobility increases the probability of finding the opposite charge carrier, thus enhancing the charge recombination. This occurrence proves the assumption that the bimolecular recombination loss is one of the major device efficiency limiting factors in the P3HT:PCBM blend prepared with different solvents.

The last step is the evaluation of the solvent influence on the charge carrier extraction. In order to evaluate the charge carrier extraction, the mobility-lifetime product $\mu\tau$ has been studied as a function of the bias current injection level. This quantity is a quality like factor, giving direct information about the competition between the charge carrier transport and the recombination mechanisms in the active layer. Both processes strongly affect the voltage bias dependence of the photocurrent and hence the efficiency of the solar cell. As clearly visible in Fig. 5.6, the charge mobility is directly proportional to the temperature for both solvents. Conversely, Fig. 5.5 shows that the charge carrier lifetime is inversely proportional with temperature. Langevin-type bimolecular recombination theory fulfills both trend providing $\mu\tau$ should be independent of the temperature [43].

The values of $\mu\tau$, measured between 300 and 330 K, for different bias currents, and in dark condition, are reported as Arrhenius plots for the oDCB and oDCB+THN solvent in Fig. 5.8. The mobility-lifetime product, at low current injection levels, that is 20 µA and 30 µA, shows a temperature-independent value of about 15 × 10^{-6} cm^2V^{-1}, in good agreement with that reported in literature [42].

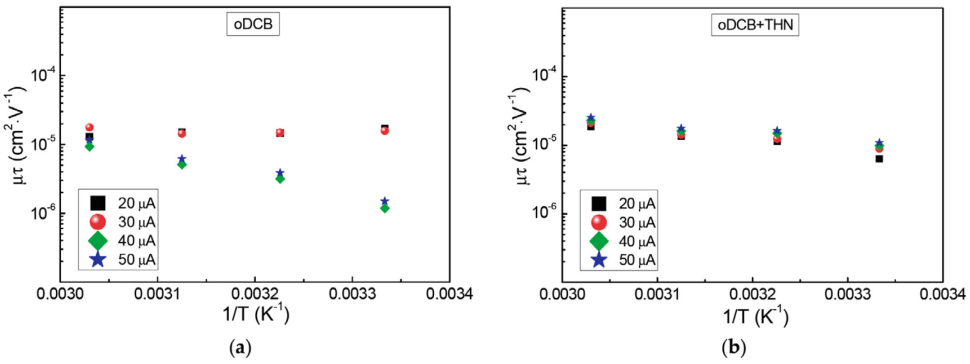

Figure 5.8 (a) Temperature dependence of the mobility-lifetime products for the blend prepared by using oDCB reference solvent. **(b)** Temperature dependence of the mobility-lifetime products for the blend prepared by using oDCB+THN solvent.

By increasing the current, the charge amount n, accumulated in the device, increases and the mobility-lifetime product becomes temperature dependent. For a bias current of 50 µA, corresponding to a charge density of 10^{16} cm^{-3} within the active layer, the $\mu\tau$ product decreases of one order of magnitude assuming a

value of about $10^{-6}cm^2V^{-1}$. This demonstrates that the charge extraction process is less efficient for the device prepared with the reference solvent, and is coherent with the lower value of J_{SC} measured for this device (Fig. 5.2 (a)).

The other type of active layer, THN additive based, show an almost temperature-independent behavior of the $\mu\tau$ product with an average value of ≈ 20×10^{-6} cm^2V^{-1} (close to that observed for the oDCB) in all the investigated current range.

The reduction in carrier mobility gives a longer carrier lifetime, as predicted by Langevin-type bimolecular recombination, where the recombination rate R_L is determined by the mobility. This result complies with the assumption that the use of the high-boiling-point additive affects positively the morphology thereby increasing the mesoscopic ordering in the donor and acceptor phases.

To sum up, the role of the solvent additives on the performance of polymer:fullerene solar cells has been investigated by using temperature-dependent fluctuation spectroscopy under dark conditions. The polymer ordering within the blend has positive effects on the measured external quantum efficiency signal, on the increase of the short circuit current and, as a consequence, of the power conversion efficiency. Such a result is also confirmed by the surface analysis performed by using atomic force microscopy measurements, that indicate a connection between an increase of the device performance and the increase of the surface roughness. The observed temperature dependencies of the charge carrier lifetime and charge velocity (i.e., the mobility) suggest that the recombination kinetics, occurring within the blend, is bimolecular and follows the Langevin theory. More in details, the carrier lifetime presents a temperature-induced reduction, while the carrier mobility increases with increasing temperature, causing an evident enhancement of the carrier recombination rate. For this reason, the use of a high-boiling-point solvent (such as THN) reduces the recombination rate at the donor-acceptor interface and increase the carrier lifetime in the films.

Following the Langevin theory, the devices with a well-ordered blend structure show temperature-independent mobility-lifetime products and, therefore, a more efficient carrier extraction process. Conversely, blends prepared with a less-ordered active layer are characterized by an increased recombination rate at the donor-acceptor interface (mainly due to the energetic disorder and charge accumulation), which leads to a drop of the mobility-lifetime products.

Author contribution The author contributed to the voltage noise-measurements of all devices. The author contributed to the discussion of the results and the implications.

CHAPTER 6
Noise properties and transport in perovskite solar cells

The past years have seen the rapid emergence of a new class of solar cell based on mixed organic–inorganic halide perovskites. The first efficient solid-state perovskite cells were reported in 2012, and five year later energy conversion efficiencies reached a promising 22.1% [47].

As in microelectronics, silicon has a combination of key features that has made it difficult to displace as the favoured photovoltaic material. Opportunities arise for technologies that promise either significantly lower processing costs or significantly higher energy conversion efficiencies. A new era of mixed organic–inorganic halide perovskites, such as $CH_3NH_3PbI_3$, offers intriguing prospects on both fronts.

The use of perovskites in photovoltaics is due to their peculiar chemical and physical properties, associated with a simple synthesis. They exhibit bandgap energies in the near-infrared close to the Shockley-Queisser ideal limit [48], long charge carrier lifetimes [49], elevated charge carrier mobilities, and diffusion lengths on the order of micrometers. Moreover, hybrid perovskites are an ideal candidate for tandem solar cells with silicon, due to the low sub-bandgap absorption and the high bandgap energies, features which suggest the potential to outperform traditional single junction silicon solar cells [50],[51].

A broad range of different fabrication approaches and device concepts compete among the highest performing devices. This diversity suggests that performance is still far from fully optimized.

In addition, a clear picture of the electrical transport mechanisms in perovskites has not been achieved. There is a wide scientific literature on the photophysics of these materials at room and high temperatures [52],[53], but the understanding of how the lowering of temperature affects the charge carrier dynamics is still scarce, as well, the comprehension of the defect structure and their impact on carrier recombination and charge transport combined with the electron–phonon scattering is still an open issue. The presence of the intrinsic defects, in particular point defects, in the absorber layer can lead to the formation of distributed recombination centers within the forbidden gap that could cause recombination losses. A side effect of the intrinsic point defects is the formation of shallow defects that produce an unintentional doping in the absorber layer.

Several approach have been proposed to reduce the effect of the recombination process, through defect states, on the device performances. For example, Shao et al. have demonstrated that the use of the fullerene material, as electron transport layer, leads to a partial deactivation of the surface and of the grain boundary charge traps, related to the perovskite absorber layer. This

also mitigates the often observed photocurrent hysteresis and increase the charge carrier lifetime and mobility [54].

In this respect, the carrier kinetic processes after optical excitation have been investigated [55], and theoretical calculations have been performed by using experimental results from millimeter-wave spectroscopy, temperature-dependent absorption spectra, , low-frequency dielectric measurements, and NMR data related to the motion of molecular cations [56]. Photoluminescence properties, under one-photon and two-photon excitation, have been also studied in $CH_3NH_3PbI_3$ microdisks, giving a more comprehensive understanding of the nonlinear effect of organic-inorganic perovskite single crystals [57].

Several experimental techniques, such as temperature dependent admittance spectroscopy or time-resolved photoluminescence decay measurements, have been used to obtain a detailed analysis of the recombination processes and defect states population. Among the non-destructive characterization techniques, noise spectroscopy has demonstrated its effectiveness in the investigation of advanced photovoltaic and innovative materials [16] [31].

In the following paragraphs, a detailed analysis of the fluctuation processes has been performed in methylammonium lead iodide ($CH_3NH_3PbI_3$) shining light both, on the temperature dependence of localization effects, including phonon coupling and charge carrier trapping and on capture and emission of the charge carriers from the defect states, that can be modeled by means of trapping/detrapping and recombination mechanisms. In particular, once a phase transition from a tetragonal to an orthorhombic structure has been observed near 160 K [58], noise measurements prove to be an efficient experimental technique, considering that no clear signature of such a transition is evident in the cell DC properties.

6.1 Materials and methods

Perovskite solar cells were prepared at the Helmholtz-Zentrum Berlin für Materialien und Energie (Germany), following the layer sequence glass/ITO/ PEDOT:PSS/$CH_3NH_3PbI_3$/$PC_{61}BM$/BCP/Ag (see Fig. 6.1).

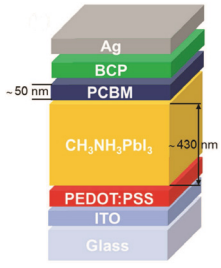

Figure 6.1 Sketch of the cross-section of the devices structure.

In the first step, patterned glass/ITO substrates were cleaned with acetone, detergent/H_2O, H_2O, and isopropanol. After a final plasma cleaning, a 60 nm thick PEDOT:PSS layer (Heraeus PH 4083) was prepared by spin-coating at 3000 rpm for 30 s. The obtained films were annealed at 150 °C for 20 min, and then transferred to inert atmosphere. A stoichiometric $CH_3NH_3PbI_3$ precursor solution, containing either 0.8 M (thin and small grained sample) or 1.1 M (thick and large grained sample) of PbI_2 (Sigma-Aldrich, 99.999%) and CH_3NH_3I (synthesized from CH_3NH_2 and HI [58], Sigma-Aldrich) in the mixed solvent γ-butyrolactone (GBL) and dimethyl sulfoxide (DMSO) with volume ratio 70/30 (v.%/v.%), was prepared under stirring at 60 °C for 12 h. The $CH_3NH_3PbI_3$ absorber undergone to several spin-coating cycles: at 1000 rpm for 10 s, 2000 rpm for 20 s, and 5000 rpm for 20 s. In the last spin-coating stage, 150 µl toluene were dripped onto the sample. After crystallization at 100 °C for 10 min, a smooth $CH_3NH_3PbI_3$ layer was obtained. The electron selective contact was formed by spin-coating a 50 nm thick $PC_{61}BM$ layer (Lumtec, 99.5%, 20 mg ml^{-1} in chlorobenzene) at 2500 rpm for 60 s. After annealing at 100 °C for 10 min, a thin layer of bathocuproine (BCP, 0.5 mg ml_{-1} in ethanol, Sigma-Aldrich) was spin-coated at 4000 rpm for 45 s. Finally 100 nm of Ag was thermally evaporated through a shadow mask at a base pressure below 10^{-7} mbar. The active area was confined to 0.16 cm^{-2} by the overlapping metal and ITO contacts. For noise measurements, samples were encapsulated in glass using a two-component epoxy.

The perovskite solar cells were characterized under a simulated solar spectrum (AM1.5G, Newport LCS-100 class ABB sun simulator). The light intensity hereby was calibrated using a Si photodiode from Fraunhofer Institute for Solar Energy Systems ISE CalLab Photovoltaic Cells. Current voltage scans were acquired in forward and reverse directions using a voltage sweep of 85 mV s^{-1}. A calibrated “ORIEL QEPVSI-b” setup was used to acquire the External Quantum Efficiency (EQE) spectra. Measurements were performed without bias illumination at short circuit. To prevent degradation by oxygen and moisture, EQE and J–V measurements were performed under inert atmosphere. A closed-cycle refrigerator controlled the temperature, whose stabilization was realized by a resistance heater controlled in a closed feedback loop (better than 1 K of achieved stability). The experimental setup consisted of a low-noise Keithley 220 dc current source for the biasing of the samples, a digital multimeter for the dc voltage drop recording, a low-noise PAR5113 Preamplifier and a dynamic signal analyzer HP35670A for the analysis of the ac voltage signal. A commercial cool white light emitting diode was used as light source for low-temperature investigations. Scanning electron images were recorded with an Hitachi S-4100 at 5 kV acceleration voltage. Top view images were acquired by removing the PCBM and BCP layers. Evaluation of the grain diameter distribution was obtained by processing top view Scanning Electron Microscopy (SEM) images with ImageJ software.

6.2 DC electrical transport properties

The current density-voltage (J-V) characteristics of the best performing device, with an efficiency of 12.1%, is depicted in Fig. 6.2 (a). In contrast to perovskite solar cells based on TiO_2 [59], the inverted device is hysteresis free [60], as evident from the shown J-V sweeps in forward and backward direction. A power point tracking algorithm additionally verifies an efficiency of 12.04% after stabilization, as indicated by the red dot. The external (EQE) and internal quantum efficiency (IQE) are shown in Fig. 6.2 (b). The integrated short-circuit current density amounts to 17.4 mA cm^{-2}, and, therefore, matched the current obtained under AM 1.5G illumination.

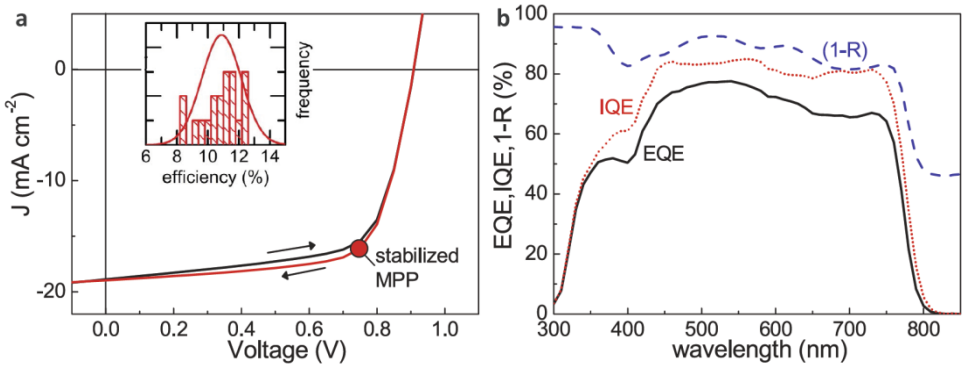

Figure 6.2 (a) Current density-voltage characteristics of the best performing device. Black and red lines refer to performed forward and backward voltage scans, respectively. The result of a maximum power point tracking after stabilization confirms the power conversion efficiency of 12% (red dot). The inset shows a histogram of the measured efficiency of 20 processed devices. **(b)** The wavelength-dependent external (EQE) and internal quantum efficiency (IQE) plotted as black and red lines. The blue dashed line refers to the measured reflection *R* as (1 − *R*).

After the typical standard test at room temperature, perovskite solar cells were probed as a function of temperature from 300 K down to 60 K. In Fig. 6.3, the temperature dependencies of the open-circuit voltage Voc (left axis) and of the short-circuit current density J_{sc} (right axis) are shown at three different light intensity.

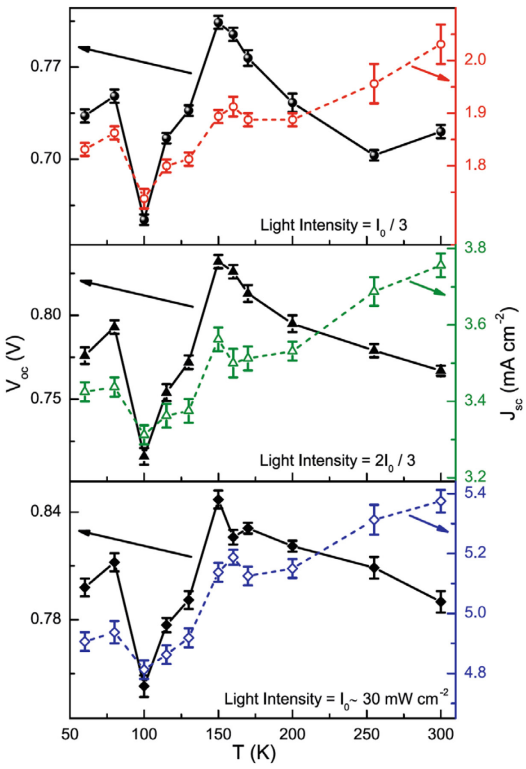

Figure 6.3 Temperature dependencies of the open-circuit voltage V_{oc} (left axis) and of the short-circuit current density J_{sc} (right axis) shown for three different light intensity.

A change in the behaviour of V_{oc} (black closed symbols), in a temperature range between 150 and 100 K, is evident, while a less pronounced effect is found for J_{sc} (coloured open symbols) independently on the light intensity. This finding suggests the occurrence of a modification in the electrical properties of the photovoltaic device. However, no precise information can be extracted on the typology of the observed phenomenon, and the structural transition from a tetragonal to an orthorhombic phase (occurring close to 160 K) could play a role in the low-temperature conduction regime of perovskite photovoltaic devices.

6.3 Noise spectral density measurements

Electronic noise analysis has been applied to gain a deeper knowledge both of the metastable state and of the correlation between electronic defect state distribution and device performance.

Phase transition analysis. Electric noise analysis starts with the measurement of voltage fluctuations S_V in a DC current biased sample. The main noise source, in semiconducting devices, is due to charge number fluctuations, therefore, a

more useful quantity for the noise spectral density is $S_I = S_V R_D^{-2}$, where R_D is the differential resistance at the DC bias point. In Fig. 6.4 (a),(c), the *I-V* characteristics are shown at two temperatures (200 and 300 K, respectively) for two different samples, namely sample #1 ("thin") and sample #2 ("thick").

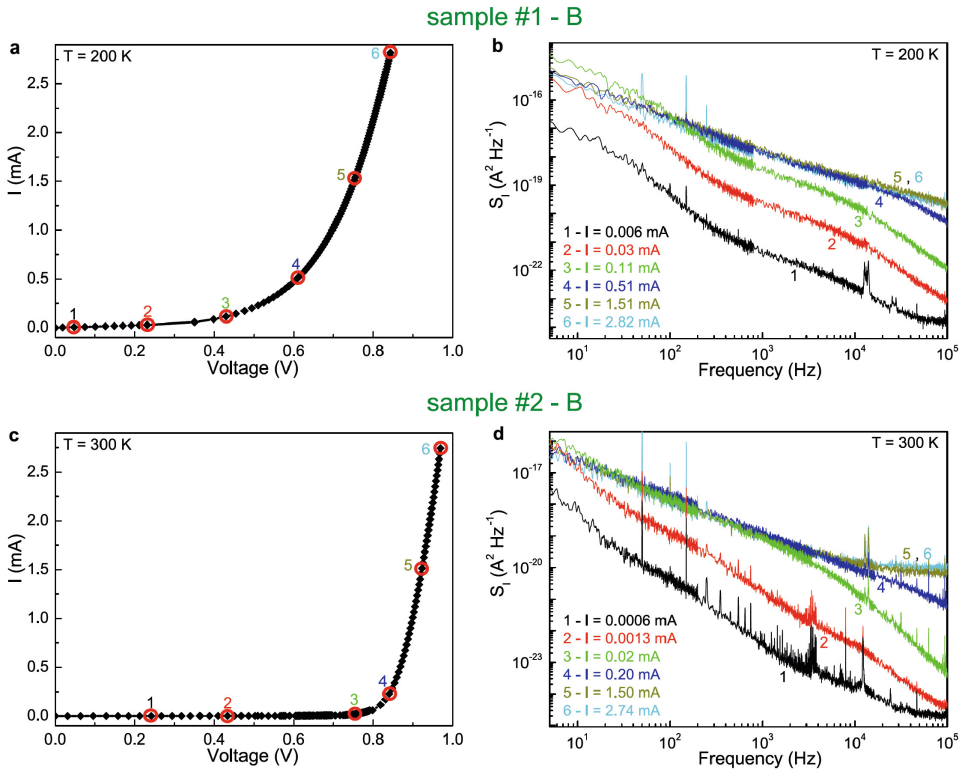

Figure 6.4 (a,c) Dark *I-V* characteristics at temperatures of 200 and 300 K for two perovskite solar cells: sample #1 device B and sample #2 device B, respectively. **(b,d)** Frequency dependence of the current-spectral density S_I for the same devices. Several bias points, at which noise spectra have been acquired, are reported.

Despite the shape of dark *I-V* curves looks different, the photoelectric parameters of the investigated devices are similar, and a general trend can be also found in the current-noise spectra. This is evident in Fig. 6.4 (b),(d), where the low-frequency dependence of S_I is shown for the same bias points of Fig. 6.4 (a),(c). It is remarkable the saturation of S_I for values higher than 0.2 mA of the applied bias, as suggested by the blue spectral traces 4 in Fig. 6.4 (b),(d). When the electric noise is saturated, a pure *1/f* component is visible, as shown by curves 5 and 6 in Fig. 6.4 (b),(d). On the opposite, in the low bias current limit, S_I exhibit two cut-off frequencies, each one specific of a change from a *1/f* to a $1/f^3$ dependence of the spectrum (spectral traces 1–3 of Fig. 6.4 (b),(d)). In particular, the highest cut-off frequency can be defined in terms of a time constant which describes the recombination phenomena associated to the defect states [31].

From noise spectroscopy, this time constant is estimated to assume temperature-dependent values between 4 and 10 μs, giving the experimental quantification of the rate constant for the physical process that produces the electric noise in perovskite solar cells. It is clear, however, that a peculiar feature of the charge carrier fluctuation mechanisms exists, indicating a crossover between distinct noise regimes. This behaviour is confirmed on several devices, and at different temperatures.

The DC bias-induced noise saturation has been observed also under light exposure. It is visible in the inset a and inset b of Fig. 6.5, where the current noise computed at a reference frequency of 90 Hz is shown as a function of the DC bias current I_{DC} and of the photogenerated current I_{ph}, at a temperature of 255 K.

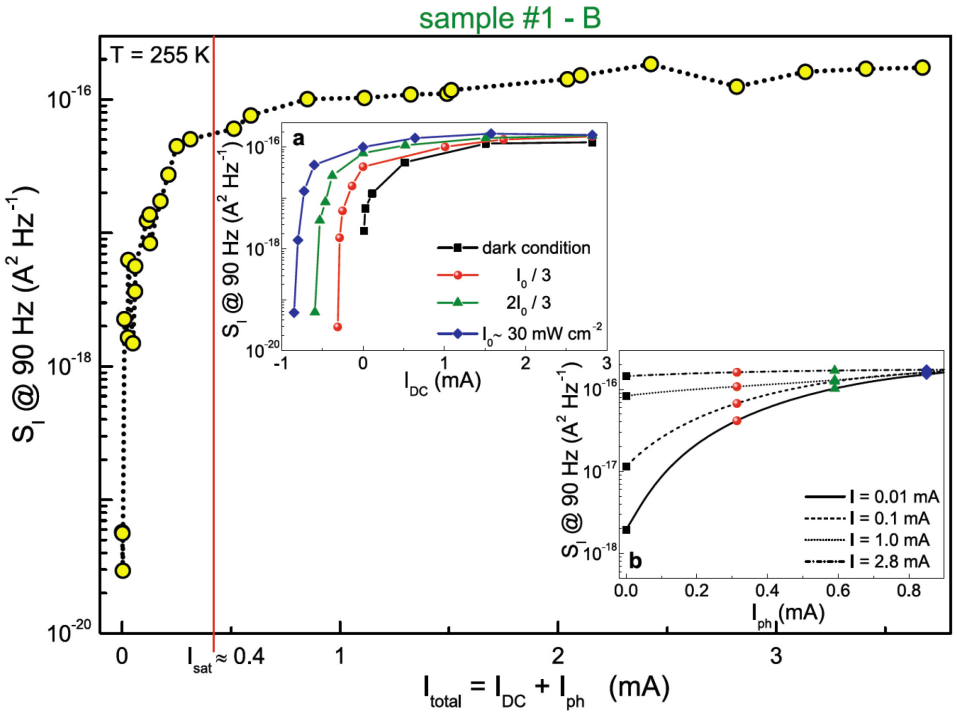

Figure 6.5 Spectral density S_I as a function of the total current for sample #1 device B at a fixed temperature of 255 K, and at a frequency of 90 Hz. A saturation of the noise amplitude is observed by varying, independently, the DC applied bias I_{DC} (inset a) and the photogenerated current I_{ph} (inset b). The noise saturation effect, arising from sum $I_{DC} + I_{ph}$, is estimated to occur near 0.4 mA.

By plotting the total current ($I_{DC} + I_{ph}$) dependence of the noise amplitude, all the experimental data distribute on a single curve (see Fig. 6.5). This proves that the measured electric noise comes from the fluctuation of total charge carriers present in the device, either photogenerated or injected by the bias leads. Moreover, a saturation of the noise amplitude is observed for currents above 0.4 mA, a value that is sample- and temperature-dependent.

An explanation of this behavior will be given using the well-known excitation-trapping fluctuation model [1] in the next paragraph. At this point, it is enough to say that free carriers, randomly trapped and released by centers with different times, control the noise process; then the generation of carriers, induced by photocurrent or DC bias, increases the trap filling until a noise saturation occurs, when all the traps are active.

Going back to estimating the overall generated noise, it is of help to measure the variance of voltage fluctuations *Var*[*V*], obtained by computing the integral of S_V in the frequency domain between [f_{min}, f_{max}] = [1, 10^5] Hz, that is the experimental bandwidth. In Fig. 6.6 the temperature dependence of *Var*[*V*], measured at large bias current (corresponding to the region of full trap activation), is shown for the investigated samples.

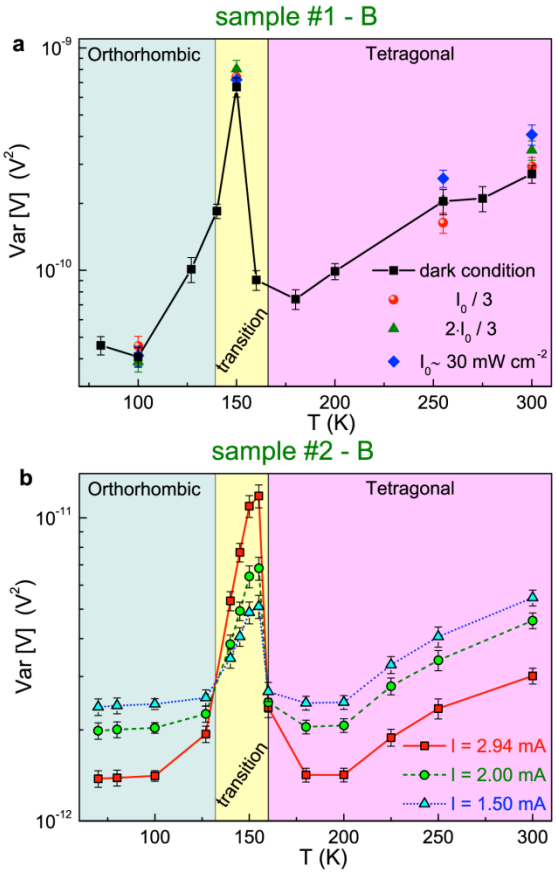

Figure 6.6 (a) Variance of the measured voltage fluctuations *Var*[*V*], at a fixed bias current value of 2.9 mA, as a function of temperature for sample #1 device B. The black squares refer to data taken in dark condition, while red circles, green triangles, and blue diamonds correspond to three different light intensity reported in the legend. **(b)** Temperature behaviour of the voltage-noise amplitude for sample #2 device B, obtained by varying the applied bias current. In both samples, the presence of a noise peak is clearly visible between 150 and 160 K.

The reported values differ by two orders of magnitude, between sample #1 and sample #2, when biased with similar currents (2.9 mA for sample #1 and 2.94 mA for sample #2). By excluding a parasitic effect of the involved interfaces, which are processed in the same way, the measured noise fluctuations are dominated by a defect related trapping/detrapping mechanism within the bulk perovskite absorber. For this reason, the lower *Var*[*V*] of sample #2 suggests a lower trap density in the device of large grain size. The finding is coherent with the reported increase of the electron-hole diffusion length with increasing grain size [61],[62]. The acquired data, both in dark and at different illumination intensity, shown in Fig. 6.6 (a), reveal the presence of a noise peak at temperatures between 150 and 160 K. This peculiarity is independent on the presence of photogenerated carriers, however it shows a clear dependence on the bias current, as visible in Fig. 6.6 (b). Interestingly, above 160 K and below 130 K, the noise level decreases by increasing the current, while the opposite behaviour is found in the temperature region around the noise peak. It is likely that the observed noise peak is related to the perovskite phase transition occurring in the temperature range close to 160 K.

The intrinsic nature of the observed temperature/noise dependence have been verified by varying the temperature, both in cooling and heating modes. No hysteretic effects are found, and no significant difference characterizes the temperature direction change. After the verification of the reproducibility of the noise peak found near 160 K, a detailed study of the voltage-noise amplitude has been done for different bias points. In order to understand the measured voltage-spectral densities, the overall noise can be expressed as the sum of two independent contributions

$$S_V(f,T) = S_I(f,T)R_D^2(T) + S_R(f,T)I^2 \tag{6.1}$$

where the first term stand for an ever-present current-noise source tied to active trapping states fluctuations induced in the photovoltaic device. As said before, this is modeled by the well-known trapping/detrapping mechanism, which induces charge carrier fluctuations and, consequently, a current noise S_I [1]. The second term of Eq.(6.1) represents a voltage-noise source that, instead, describes a resistance network fluctuation mechanism S_R, occurring in the perovskite phase-transition region where metastable states between local resistive states are established. While conventional Si-based solar cells have already shown the presence of trapping-detrapping related processes [27], resistive-induced fluctuators are commonly found in random network systems [17] but are unforeseen in photovoltaic materials. In Fig. 6.7 (a),(c), the evaluated voltage-spectral density amplitudes are shown in the low (orthorhombic) and high (tetragonal) temperature regions, respectively.

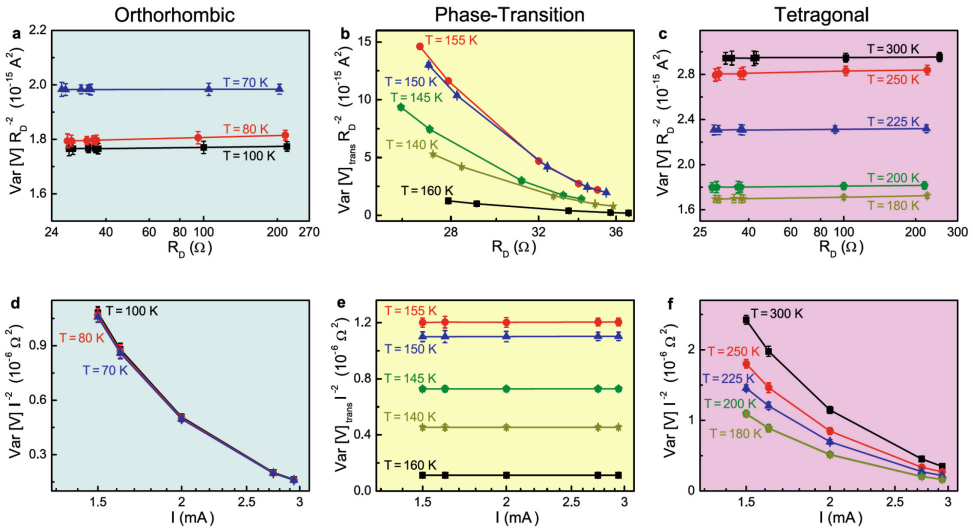

Figure 6.7 (a,c) Normalized noise amplitude *Var* $[V]R_D^{-2}$ for several values of the differential resistance. **(d,f)** Bias current dependence of the normalized noise $Var[V]I^{-2}$ **(b,e)** The behaviour found for the tetragonal (T > 160 K) and the orthorhombic (T < 130 K) phases is no more observed in the transition region (160<T<130 K). The excess noise contribution $Var[V]_{trans}$ has been reported.

The experimental results reveal a direct proportionality of the noise level with the differential resistance squared, and are coherent with the presence of a current-noise source alone (first term of Eq. (6.1)). This noise contribution increases with temperature above 200 K, while, below 200 K, is substantially constant. However, in the region around 160 K, the experimental behaviour is completely different and is characterized by the appearance of an excess noise component, which can be evaluated by subtracting from the measured noise level the constant current-noise term. The values of this excess noise contribution, shown in Fig. 6.7 (b),(e) as $Var[V]_{trans}$, seem to scale well with the applied bias squared I^2 and, conversely, have no relation with R_D^2 .

The unexpected additional noise observed near 160 K can be explained in terms of structural reorganization of the perovskite material. In this framework, a random distribution of microscopic phases occur, to which a random resistor network can be associated. The resistors fluctuate randomly between the values characteristic of the two perovskite phases, giving rise to a *1/f* noise with a quadratic bias current dependence. This is well shown in Fig. 6.7 (e), where the excess noise level scaled with I^2 exhibits a constant value, different for the specific temperatures investigated. The highest value is found at 155 K, indicating this as the structural transition temperature of the perovskite compound. Moreover, the quadratic bias scaling is missing outside the phase-transition region, confirming the proposed model. As a consequence, from the noise point of view, the low-temperature crossover between the tetragonal and orthorhombic phases can be identified by the change from a trapping/detrapping to a resistance fluctuation mechanism. The structural

reorganization of the microscopic metastable states, occurring in the transition region, may be characterized by long-term relaxation processes, which are probably due to the two turning points (around 150 and 100 K) observed in the V_{oc} temperature dependence (see Fig. 6.3 for details).

Electronic defect state distribution *vs* device performance analysis. Under charge carrier injection and at low frequencies, the ac equivalent electric circuit of the solar cell is a simple parallel connection between the differential resistance $R_D = dV_F/dJ$ and the chemical capacitance C_μ [31]. More in detail, $V_F = V - R_sJ$ is the forward bias voltage corresponding to the splitting of the quasi-Fermi levels for electrons and holes (E_{Fn} and E_{Fp}, respectively) under light illumination or current biasing. C_μ is a capacitance containing the contribution of the minority charge carriers stored in the device. In this contest, the effective lifetime τ_{eff} is expressed as the product R_DC_μ and can be estimated by the noise frequency dependence, remembering that thetrap-assisted recombination phenomena in the device is dominant [31]. The trapping of the charge carrier in the defect states can lead to a nonradiative recombination process or to an emission of the charge in the conduction band. The trapping/detrapping processes cause a number fluctuation of the charge carriers and, therefore, a current-noise contribution that can be measured [27]. In terms of spectral density, the resulting current-noise source can be expressed as [31]

$$S_I(f) = \frac{K}{f^\gamma}\frac{1}{1+\left(\frac{f}{f_x}\right)^2} + S_0 \tag{6.2}$$

where K is the temperature-dependent noise amplitude, γ is an exponent close to unity [1], f_x is defined as $(2\pi\tau_{eff})^{-1}$ [27], and S_0 is the background noise due to the readout electronics. This expression of the spectral density clearly shows the role of the effective lifetime τ_{eff} term. The good agreement between noise data and the fitting formula of Eq. (6.2) is visible in Fig. 6.8 (a), where S_I, measured at a fixed bias current of 0.02 mA, is reported at three different temperatures. The best fitting curves [red dashed lines] are obtained with values of f_x varying from (15.3 ± 0.3) kHz at 300 K to (35.1 ± 0.8) kHz at 127 K. This suggests that the effective lifetime decreases by lowering the temperature, from a value of ≈10 μs at room temperature to ≈ 4 μs in the low-temperature range. The τ_{eff} temperature dependence is depicted in Fig. 6.8(b), where two activated behaviors are found as evidenced by the straight lines in the Arrhenius plot.

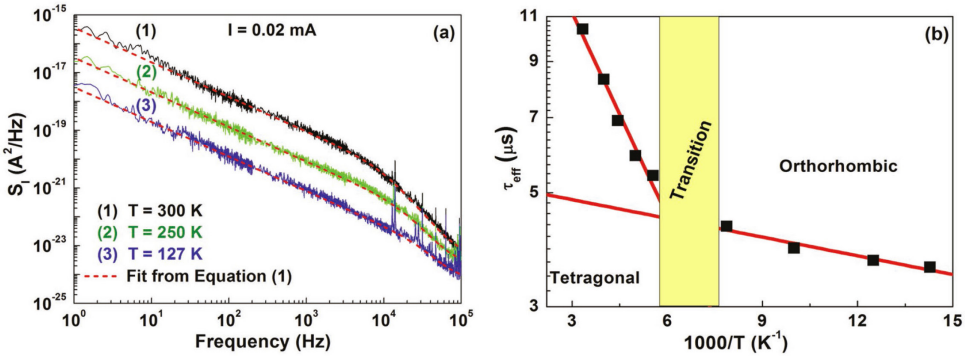

Figure 6.8 (a) Current-noise spectra of a typical investigated perovskite photovoltaic device at a fixed bias current value (0.02 mA) and at three different temperatures. The best fitting curves (red dashed lines) are obtained with Eq. 6.2. **(b)** Arrhenius plot of the effective lifetime coefficient τ_{eff} (70 k < T < 300 K). Two distinct behaviors are evident: in the room-temperature tetragonal and in the low-temperature orthorhombic phases.

More in details, two distinct activation energies are observed in the low-temperature orthorhombic [E_a = (25.5 ± 0.5) meV] and in the room-temperature tetragonal [E_a = (53 ± 1) meV] perovskite-material phases. Similar values of τ_{eff} and of the activation energies have been already reported on $CH_3NH_3PbI_3$ solar cells by using impedance spectroscopy measurements [63]. The structural phase transition strongly influences the distribution and the types of the defect states within the device. As a consequence, the electric field profile, the charge carrier collection, and the recombination kinetics must be investigated. It is worth to note that the perovskite material is characterized by several types of point defects, such as interstitials (I_I), vacancies (V_{Pb}), cation substitutions (MA_{Pb}, Pb_{MA}), and antisite substitutions (Pb_I, I_{Pb}). Some of these defects act as intrinsic acceptor and/or donor shallow defects, thus leading to an uncompensated doping, while others, characterized by a higher formation energy, act as deep defect states that influence the recombination kinetics and, therefore, the device performances. Moreover, besides the interstitial Pb_I and I_{Pb} point defects, even the fragments of CH_3NH_3 and their possible complexes with the iodine atoms can lead to the formation of additional deep traps [64].

The next step is the determination of the electronic density of states (DOS) distribution with traps. At zero bias, the depletion capacitance C_{depl}, at the interface between the perovskite layer and the metal contact, is function of the geometric contribution of the PCBM and $CH_3NH_3PbI_3$ materials [65]. By increasing the bias voltage, the number of charge carriers accumulated in the active layer increases too, thus increasing the chemical capacitance value C_μ, as compared to C_{depl}. Taking into account the zero-temperature approximation of the Fermi function at an occupancy >1%, the chemical capacitance complies with the shape of the electronic DOS [66]. It is possible to evaluate the electronic DOS at a given level of the E_{Fn} as: $g(E) = C_\mu q^{-2} d^{-1}$, where q and d are the elementary charge and device thickness, respectively, and the capacitance per unit area C_μ=

τ_{eff} R_D^{-1} [67]. The values of the DOS distribution, derived from noise measurements through τ_{eff}, are shown in Fig. 6.9 (a) at a temperature of 300 K and 250 K.

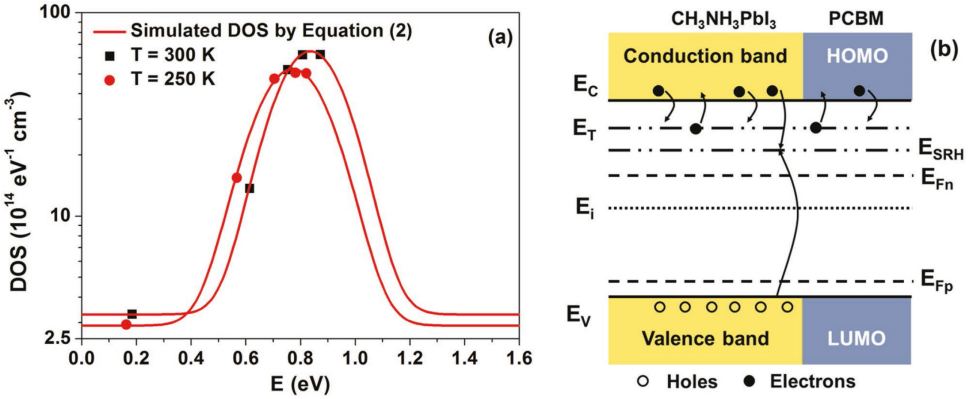

Figure 6.9 (a) Electronic density of states (DOS) extracted from noise measurements at 300 K (black squares) and at 250 K (red circles), respectively. The best fitting curves, obtained with Eq. (6.3), are shown as red solid lines. **(b)** Energy-band diagram of the perovskite-based device illustrating the carrier recombination and trapping/detrapping processes.

The DOS disordered semiconductors is usually modeled with a Gaussian distribution [68] as

$$g(E) = \frac{N_0}{\sqrt{2\pi}\sigma_n} \exp\left[-\frac{(E-E_0)^2}{2\sigma_n^2}\right] + g_0 \qquad (6.3)$$

where N_0 is the electron density per unit volume, E_0 is the center of the DOS, σ_n is the disorder parameter, and g_0 represents the DOS background level. The best fitting curves resulting from Eq.(6.3) are shown in Fig. 6.9 (a) as red solid lines. The best fitting parameters are: N_0 = (1.9 ± 0.1) × 10^{15} cm^{-3}, σ_n = (124 ± 6) meV, and E_0 = (0.84 ± 0.05) eV for 300 K; N_0 = (1.6 ± 0.1) × 10^{15} cm^{-3}, σ_n = (120 ± 6) meV, and E_0 = (0.77 ± 0.05) eV for 250 K.

The resulting values of σ_n are higher than those reported in literature (≈90 meV for the perovskite solar cell with PCBM material as electron transport layer) [68]. This could be related to the large energy disorder in the device, where the presence of the subgap states [68] causes non-negligible recombination losses. The role of σ_n can be also observed by taking into account the Urbach energy U_E of the tail states that can be estimated by the quantum efficiency data [69]. The evaluation of U_E for the tail states is ≈31 meV with a bandgap E_g of 1.59 eV for the $CH_3NH_3PbI_3$ compound. Also this value is larger than what is reported in literature (≈16 meV) and it is a further evidence of the broad distribution of the tail states inside the forbidden gap [70]. Cody et al. suggest that the total

disorder can be seen as the sum of two terms, thermal/dynamic disorder and static disorder [71].

The thermal disorder is due to the excitations of phonon modes, while the static disorder is due to inherent structural disorder. As already observed by Singh et al. with both absorption and photoluminescence measurements performed on the perovskite material, in the room-temperature tetragonal phase the main contribution to the disorder can be related to the thermal disorder whereas the static disorder results to be dominant at lower temperatures (T < 60 K) [72]. At both the investigated temperatures, the total electron density population N_0 is lower than what found in literature for the best performing $CH_3NH_3PbI_3$ solar cell (η = 19%), i.e., 10^{16}–10^{17} cm^{-3} [68]. This means that the occupation of the highest energy defect states in the DOS tail results to be extremely limited by the presence of defects that influence the recombination process. As a consequence, the N_0 value estimated by the noise measurements should be attributed to the density of SRH traps.

The estimated value of g_0 is ≈ 3.1 × 10^{14} eV^{-1} cm^{-3} at 300 K and slightly decreases with temperature. Assuming that, at low bias currents, the main contribution to the capacitance is related to C_{depl} and a one-side abrupt step junction approximation, the depletion zone width, extended within the perovskite material, can be expressed as [32] $C_{depl} = \sqrt{\mathrm{A}^2 \mathrm{q} \epsilon_0 \epsilon_\mathrm{P} \mathrm{N} / 2(\mathrm{V_{bi}} - \mathrm{V_F})}$, where ε_0 = 8.85 × 10^{-14} F cm^{-2} is the vacuum permittivity, A is the area of the active layer, and ε_P = 21.2 is the relative dielectric constant of the $CH_3NH_3PbI_3$ compound. By estimated the value of V_{bi} from the J–V curves under dark conditions [69], the value of the uncompensated doping concentration N = (2.1 ± 0.1) × 10^{14} cm^{-3} can be extracted. This is in good agreement with the intrinsic doping concentration (10^9–10^{14} cm^{-3}), reported in literature for the perovskite material, and considers the quality of the absorber layer. In the $CH_3NH_3PbI_3$ compound a point defects related to Pb or I atom vacancies give the main contribution to the unintended doping observed in the absorber material that can be either p-type or n-type, respectively. At the interface, the PCBM material results to be homogeneously distributed throughout the film at perovskite grain boundaries and pushes the electron extraction. Therefore, the recombination phenomena occur at the interface perovskite/PCBM and extend within the $CH_3NH_3PbI_3$ compound. The presence of the exponential tail from the conduction band E_C can be modeled as shallow defect states N_{tot}, which act as trapping sites and are located at the energy level $E_C - E_T$. On the other hand, a small fraction of N_{tot}, defined as N_{SRH}, acts as deep SRH-type recombination centers [27]. The SRH defect states, located above the intrinsic Fermi level E_i, at an energy depth $E_C - E_{SRH}$ below the conduction band edge, give the major contribution to the recombination kinetics. An energy-band diagram representing the electronic transitions between the E_T and the E_{SRH} energy levels with the conduction and valence bands is shown in Fig. 6.9 (b). Under charge carrier injection, the electron quasi-Fermi level E_{Fn} moves across these electronic states influencing

their occupation probability. The emission probabilities $e_{n,p}$ and the capture probabilities $c_{n,p}$ for the electron and hole traps influence the density of the filled traps n_t so that the current fluctuation can be measured [27].

The current-noise variance *Var*[*I*], calculated by integrating S_I over the experimental frequency bandwidth, is the useful statistical quantity to estimate the influence of the electronic transitions between the defect states and the valence and conduction bands. The total current (dc bias plus photogenerated) dependence of *Var*[*I*] is reported in Fig. 6.10, for several temperatures between 300 K and 70 K.

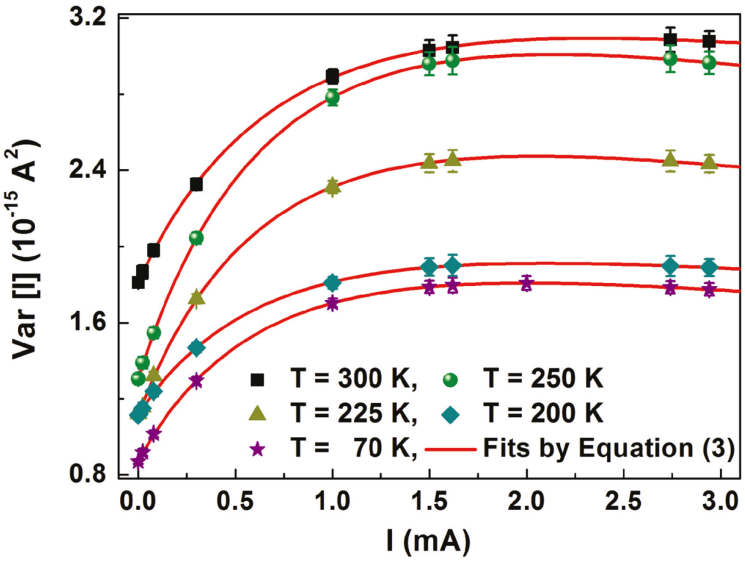

Figure 6.10 Current dependence of the noise amplitude in the temperature range between 300 K and 70 K. The best fitting curves, using Eq. (5.4), are shown as red solid lines. The values for I = 0 represent the dark noise contributions.

For all the investigated temperatures, an increase of the total current produces a rise of the noise amplitude up to a saturation level $Var[I]_{sat}$. It seems that the charge carrier injection produces a filling of the defect states in the solar cell. The explanation of this behavior can be given in terms of a theoretical model, formulated by combining trapping/detrapping related processes and charge carrier recombination phenomena. Following this hypothesis, the data in Fig. 6.10 have been fitted and shown as red solid lines, using the expression

$$\mathrm{Var}[I] = A_1 \frac{1}{\left(1+\frac{\mathrm{I}}{\mathrm{I}_0^{\mathrm{light}}}\right)^2} + A_2 \frac{1}{\left(1+\frac{\mathrm{I}}{\mathrm{I}_\mathrm{A}}\right)^2} \qquad (6.4)$$

where A_1 and A_2 stand for the amplitudes of the current fluctuations due to the recombination and trapping/detrapping mechanisms, $I_0^{\text{light}} = \frac{q}{\tau_{\text{eff}}} Ad \frac{e_n}{c_n}$ and $I_A = \frac{q}{\tau_{\text{eff}}} Ad \frac{N}{k}$ with A the sample area and d the thickness [27]. From the estimation of the fitting parameters of Eq. (6.4) it is possible to evaluate the N_{tot} and the N_{SRH} trap densities as [27]

$$N_{\text{SRH}} = \frac{A_1 I_0^{\text{light}}}{Ad}\left(\frac{\tau_{\text{eff}}}{q}\right)^2 \text{ and } N_{\text{tot}} = \frac{A_2 I_A}{Ad}\left(\frac{\tau_{\text{eff}}}{q}\right)^2 \tag{6.5}$$

It is worth noting that the proposed model, which takes into account the electronic transitions between the defect states and the conduction and valence bands, cannot be applied because in the temperature range where the phase transition occur, the spectral density of voltage fluctuations S_v is dominated by the resistance fluctuation mechanism instead of current fluctuations. The Eq. (6.5) allows the estimation of the temperature dependence of the trap densities N_{SRH} and N_{tot}, which are reported in Fig. 6.11 (a),(b), showing their increase with increasing temperature.

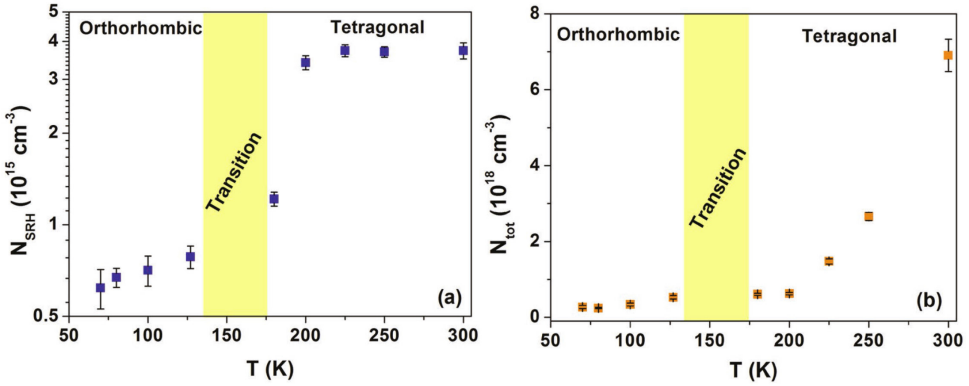

Figure 6.11 (a) Temperature dependence of the recombination trap density N_{SRH} in the band tail. **(b)** Temperature dependence of the fluctuating trap density N_{tot} in the band tail.

The trend is consistent with the evidence that the noise amplitude, proportional to the density of the traps within the device, increases with the temperature as already seen in Fig. 6.8 and Fig. 6.10. In the orthorhombic phase of the perovskite material, the density of defect states N_{SRH} seems to be saturated at a value of ≈ 7 × 10^{14} cm^{-3} (see Fig. 6.11(a)). In the tetragonal phase, after the structural modification of the $CH_3NH_3PbI_3$ absorber layer, a considerable increase of the N_{SRH} value is observed. At room temperature N_{SRH} is ≈ 4 × 10^{15} cm^{-3}.

The temperature influences also the density N_{tot} related to the band tail defect states. Below 200 K, the N_{tot} stays quite constant at ≈ 3 × 10^{17} cm^{-3} , then begins to increase reaching a value of ≈ 5 × 10^{18} cm^{-3}. This temperature dependence suggests that the trap states are intrinsic to the perovskite and varying with temperature, may be related to thermally activated atomic vacancies, a common type of point defects in perovskite structures. In addition, the estimated N_{tot} is in good agreement with values reported in literature (10^{17} - 10^{19} cm^{-3}) [73].
In the perovskite solar cell, the current fluctuations are associated to the trap-assisted recombination processes and modeled by two energy levels, which act as trapping E_T and recombination E_{SRH} centers. Under low charge carrier injection, $\tau_{\mathrm{eff}} = \tau_{\mathrm{n}}(1 + I_0 / I_{\mathrm{A}})$, where $\tau_{\mathrm{n}} = (\mathrm{c_n N_{tot}})^{-1}$ [27], and c_n is defined as the product of the electron capture cross-section σ_n and its thermal velocity v_{th}, that varies in temperature as $\sqrt{T}$. Therefore, the σ_n values can be estimated once the temperature dependence of N_{tot} has been considered. The σ_n versus T relationship is shown in Fig. 6.12.

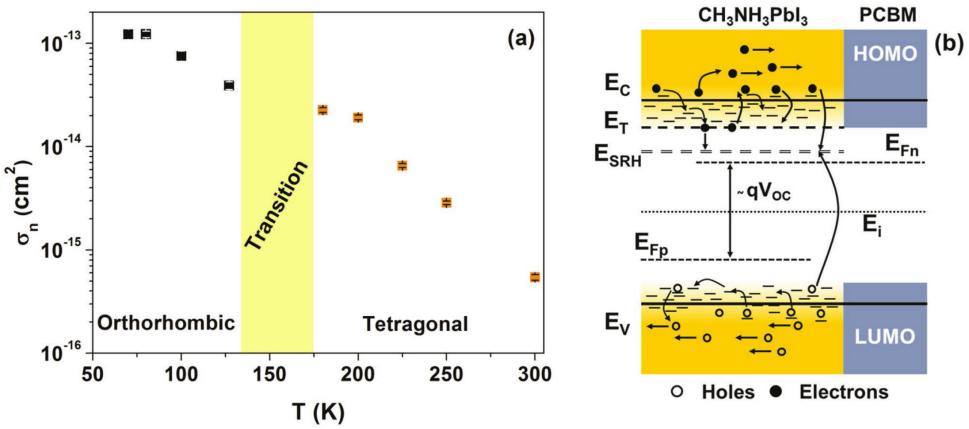

Figure 6.12 (a) Temperature dependence of the electron capture cross-section σ_n. **(b)** Energy-band diagram of the perovskite-based device showing the electronic transitions between the traps, the conduction and valence bands in a two stage model for deep states.

Different studies report the decrease of σ_n with the increase of the temperature [74]. This decay trend indicates that the electron capture in the defect states is phononassisted demonstrating that the phonon scattering influences the charge carrier transport in the $CH_3NH_3PbI_3$-based solar cells. As reported in literature, the transport mechanism occurs by multiple trapping process and hopping transport through defect sites [74]. The trapping/detrapping and recombination mechanisms between shallow and deep defect states under charge carrier injection are shown in Fig. 6.12 (b). In this respect, Gibb et al. proposed a model which describes the interactions between the charge carriers and the phonons in presence of distributed defect states: the capture of the charge carrier occurs in two stages in which the electron is first captured by a shallow defect (localized at

$E_C - E_T$) and then it is emitted in the band tail state or thermalize to a deeper ground state ($E_C - E_{SRH}$) via a multiphonon emission process [74]. Therefore, σ_n can be expressed as

$$\sigma_{\mathrm{n}} = \frac{v}{v_{\mathrm{th}} N_{\mathrm{c}}} \mathrm{e}^{\left(\frac{E_C - E_{\mathrm{T}}}{k_B T}\right)} + \sigma_{\mathrm{c}} \tag{6.6}$$

where v is the capture rate (assumed independent on T) into a deep level from the shallow center and N_c is the effective density of states in the conduction band which varies as $T^{3/2}$. Here, v_{th} and N_c depend on the temperature, so that $\sigma_{\mathrm{n}} \approx T^{-2} \exp[(\mathrm{E_c} - \mathrm{E_T}) / k_{\mathrm{B}} T]$ at high temperatures. Conversely, by decreasing the temperature σ_n approximately matches σ_c. This means that, at any time, shallow level capture is followed by a capture into the deep defect states. This process leads to a loss of the energy of the carrier with the emission of phonons during the thermalization.

The structural phase of the absorber material affects the dynamics of the defect states involved in the trapping mechanisms. The Arrhenius plot of $\sigma_n T^2$ for the perovskite solar cell reveals a clear change of the slope when a structural modification occurs (see Fig. 6.13(a)).

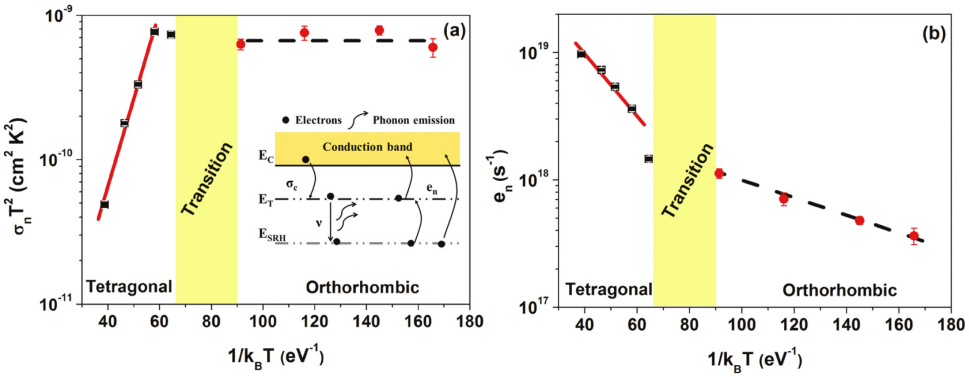

Figure 6.13 (a) Arrhenius plot of $\sigma_n T^2$ for the shallow defect states at 140 meV. The inset shows the electron capture and emission mechanisms from the conduction band caused by the shallow and deep defect states with the multiphonon emission process. **(b)** Arrhenius plot of the e_n for the deep defect states at 220 meV below the conduction band edge.

In particular, in the tetragonal phase of the $CH_3NH_3PbI_3$ material, the quantity $\sigma_n T^2$ is characterized by a constant dependence of type $\sigma_c = \sigma_0 T^{-\alpha}$ where $\alpha = 2$. As a conseguence, the capture process of the charge carriers is a cascade capture mode characterized by a strong phonon interaction [74]. Moreover, in the orthorhombic phase, the exponential contribution in Eq. (6.6) is dominant, leading to an estimation of the energy depth of the shallow defects as $E_C - E_T = (141 \pm 4)$ meV. The emission probability from deep states is

$e_n = N_c c_n \exp[-(E_c - E_{SRH})/k_B T]$ where $c_n = v_{th}\sigma_n$. In Fig.6.13 (b) the Arrhenius plot of e_n from 70 to 300 K is reported. For T > 160 K, deeper defect states are located at about 74 meV below the energy depth of the shallow centers, and active SRH-type recombination centers lie at ≈220 meV below the conduction band edge, consistent with the estimations reported before. Conversely, when the structure of the absorber material switches to the orthorhombic phase, the dominant recombination kinetics can be attributed to shallow defects located at ≈15 meV below the band edge, with a defect density of ≈7 × 10^{14} cm^{-3}. The observed cascade capture process indicates that the trapping of the charge carriers is phonon assisted directly followed by their recombination. Usually the shallow defects do not take part to the recombination processes and contribute to the long diffusion length and high open-circuit voltage of the perovskite solar cells. However, their dynamics together with the electron–phonon interactions in presence of the deeper states leads to an increase of the nonradiative recombination pathways with a negative influence on the solar cell performance.

Solar cell performance depends strongly on the recombination kinetics and the present defect states. To further investigate, two distinct perovskite solar cells have been fabricated: the first sample shows an average grain diameter d_{grain} of 370 nm and a thickness of 430 nm (large grained), while the second sample, shows an average grain diameter of 150 nm and a thickness of around 210 nm (small grained).

A clear correlation between the noise amplitude and the N_{SRH} defect density, estimated with the model of Eq. (6.5), for the large and the small grained sample can be observed in Fig. 6.14 (a). Samples based on smaller $CH_3NH_3PbI_3$ grains are characterized by a greater value of the $Var[I]_{sat}$ compared to the solar cells with large $CH_3NH_3PbI_3$ grains. Moreover, the defect density N_{SRH} decreases with an increase of the grain diameter suggesting that the recombination losses can be related to the defects/impurities in the crystal bulk and/or along the grain boundaries of the perovskite material.

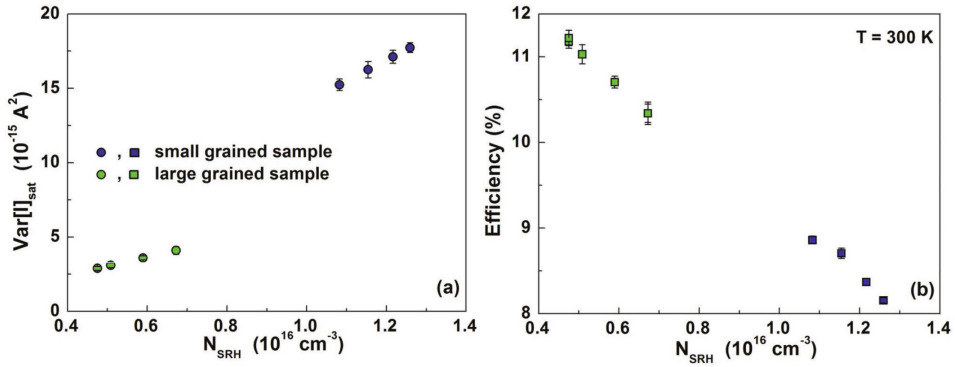

Figure 6.14 (a) Experimental value of the saturated current-noise level *Var*[*I*]sat as a function of the SRH defect density N_{SRH} (colored circles). **(b)** Correlation between the room-temperature power conversion efficiency and the N_{SRH} defect density (colored squares). Blue symbols refer to the small grained sample while green symbols refer to the large grained sample.

As a further evidence of this correlation, an increase of the U_E value, estimated by the quantum efficiency data [69], with decreasing of the grain size of the absorber layer has been observed. This finding follows the results reported in literature, where an increase of the electron–hole diffusion length, longer lifetime, and smaller N_{SRH} density is attributed to the growth of grain size of the perovskite material from polycrystalline to single crystal thin films [62],[75].

In Fig. 6.14 (b), the power conversion efficiency values as a function of the N_{SRH} defect density for both the solar cells investigated are reported. Large grained devices show higher value of η and, therefore, lower recombination losses through N_{SRH} centers compared to the devices with thinner absorber layer and smaller grain sizes.

In conclusion, a detailed temperature characterization of structural phase transition, of defect states and their energy distribution in the organic–inorganic hybrid perovskite solar cells have been performed under dark conditions and under light illumination. The temperature dependence of the carrier lifetime, extracted by the noise spectra, evidences the structural phase transition of the perovskite material at 160 K between the orthorhombic and the tetragonal phases, thus validating the low frequency noise spectroscopy as an effective and nondestructive tool. The measured electronic density of states distribution evidences a large energy disorder in the device. Moreover a clear correlation between the morphological structure of the $CH_3NH_3PbI_3$ grains, the energy disorder of defect states, and the device parameters in the perovskite solar cell has been demonstrated.

Author contribution The author contributed to the voltage noise-measurements and the DC transport investigations of all devices. The author contributed to the discussion of the results and the implications.

CHAPTER 7
Conclusions

In this thesis, electrical transport and noise properties have been investigated in different materials and devices by means of noise spectroscopy.

Starting from iron-based superconductors, pristine and aged FeSe and $FeSe_{0.5}Te_{0.5}$ thin films exhibit different behaviors, evidencing the presence of unusual noise properties that are correlated with modifications of the charge carrier conduction.

The *1/f* noise component of the aged FeSe compound shows an unusual bias current dependence in the low-temperature region, with an evident change from a quadratic to a linear behavior. This is associated to the occurrence of nonequilibrium universal conductance fluctuations, and is known to be the distinctive feature of weak-localization effects. The presence of aging-induced scattering centers in the FeSe compound is confirmed by modeling the low-temperature resistance with a weak-localization theory.

Electric transport and voltage-noise measurements performed in different polymer/CNTs composites prove that these systems can be regarded as random resistor networks, where the resistors are located at the junctions between carbon nanotubes and the nanotubes themselves connect different junctions. Independent of the polymeric matrix considered, the electrical conductivity of the compounds is influenced by the tunneling resistance, due to the nanotubes interconnections, in the low-temperature region. On the other hand, above a crossover temperature, different for each of the investigated composites, a thermal activation above the barriers becomes more favorable and dominates the current transport. The transition between these two regimes is discovered by noise spectroscopy, which evidences, in conducting composites, a temperature-driven universal crossover from a two-level tunneling fluctuation process to percolative resistance fluctuations.

Next, the study of fluctuation mechanisms has been applied to the investigation of the properties of the defect states in silicon-based solar cells. Characteristic parameters of the dominant defect centers, as extracted by noise analysis, are in good agreement with literature data. A theoretical model has been formulated to explain the nature of current fluctuations in solar cells. The applicability of the proposed model has been verified on pristine and artificially degraded Si-based devices. Differences between dark and photo-induced noise have been interpreted in terms of a Shockley-Read-Hall theory. In particular, a combination of trapping/detrapping related processes and charge carrier recombination phenomena has been considered to explain the current fluctuation mechanisms. In pristine cells, the energetic position and the symmetric ratio are consistent with the boron-oxygen complex defect, while in degraded devices, the total trap density increases with the fluence of proton

irradiation and seems to be directly related to a decrease of the power conversion efficiency.

Finally, a detailed temperature characterization of defect states and their energy distribution in the organic–inorganic hybrid perovskite solar cells have been performed under dark conditions and under light illumination. Under charge carrier injection, the temperature dependence of the carrier lifetime, extracted by the noise spectra, proves the structural phase transition of the perovskite material at 160 K between the orthorhombic and the tetragonal phases.

Above 160 K (in the tetragonal phase) and below 130 K (in the orthorhombic phase), the electric noise is generally produced by a trapping/detrapping process. Resistance fluctuations, instead, are dominant in the phase-transition region, near the noise level peak. When the active traps are filled by the charge carrier generation, the trapping noise contribution saturates. Conversely, the amplitude of resistance fluctuations increases with the squared bias current, revealing the existence of a metastable state in the crossover between the tetragonal and orthorhombic structures of the perovskite compound. This metastable state may be attributed to a random distribution of microscopic phases.

The accumulated data on *1/f* noise let us conclude that no *1/f* universal spectrum exists. The spectra of *1/f* noise in different systems are different, varying even from sample to sample of one and the same material, and depend on temperature and other conditions.

The variety of investigated devices and materials validate the soundness of the noise spectroscopy as an effective tool for electric transport analysis.

Acknowledgments

Completion of this doctoral dissertation was possible with the support of several people.

I would like to thank my supervisor, Prof. Sergio Pagano. He has taught me how good experimental physics is done.

I would like to thank Dr. Carlo Barone for his great support and patience.

I would like to thank Salvatore Abate for his valuable technical expertise.

I would like Dr. Giovanni Landi for his concrete collaboration.

I also would like to thank Prof. Heinrich C. Neitzert and Prof. Bernd Rech for giving me the opportunity to spend my Erasmus+ Traineeship period in Berlin (Germany) at the Helmholtz-Zentrum Berlin für Materialien und Energie.

Finally, I would like to thank my wife Manuela for supporting me every day, and all the people that I have met during my doctorate spent both in Salerno and in Berlin.

Bibliography

[1] S. Kogan, *Electronic noise and fluctuations in solids*. Cambridge University Press 1996, 1996.

[2] J. F. Ge *et al.*, "Superconductivity above 100 K in single-layer FeSe films on doped SrTiO3," *Nat. Mater.*, vol. 14, no. 3, pp. 285–289, 2015.

[3] C. Barone, S. Pagano, I. Pallecchi, E. Bellingeri, M. Putti, and C. Ferdeghini, "Thermal and voltage activated excess 1/f noise in FeTe0.5Se 0.5 epitaxial thin films," *Phys. Rev. B - Condens. Matter Mater. Phys.*, vol. 83, no. 13, 2011.

[4] Y. Imai, Y. Sawada, F. Nabeshima, and A. Maeda, "Suppression of phase separation and giant enhancement of superconducting transition temperature in FeSe 1− x Te x thin films," *Proc. Natl. Acad. Sci.*, vol. 112, no. 7, pp. 1937–1940, 2015.

[5] C. Barone, E. Bellingeri, M. Adamo, E. Sarnelli, C. Ferdeghini, and S. Pagano, "Electric field activated nonlinear 1/f fluctuations in Fe(Te, Se) superconductors," *Supercond. Sci. Technol.*, vol. 26, no. 7, 2013.

[6] C. Barone *et al.*, "Nonequilibrium fluctuations as a distinctive feature of weak localization," *Sci. Rep.*, vol. 5, 2015.

[7] P. A. Lee and T. V. Ramakrishnan, "Disordered electronic systems," *Rev. Mod. Phys.*, vol. 57, no. 2, pp. 287–337, 1985.

[8] W. Xue and T. Cui, "Thin-film transistors with controllable mobilities based on layer-by-layer self-assembled carbon nanotube composites," *Solid. State. Electron.*, vol. 53, no. 9, pp. 1050–1055, 2009.

[9] B. P. Singh *et al.*, "Designing of multiwalled carbon nanotubes reinforced low density polyethylene nanocomposites for suppression of electromagnetic radiation," *J. Nanoparticle Res.*, vol. 13, no. 12, pp. 7065–7074, 2011.

[10] O. Valentino *et al.*, "Influence of the polymer structure and nanotube concentration on the conductivity and rheological properties of polyethylene/CNT composites," *Phys. E Low-Dimensional Syst. Nanostructures*, vol. 40, no. 7, pp. 2440–2445, 2008.

[11] L. Guadagno *et al.*, "Mechanical and barrier properties of epoxy resin filled with multi-walled carbon nanotubes," *Carbon N. Y.*, vol. 47, no. 10, pp. 2419–2430, 2009.

[12] C. Barone *et al.*, "Experimental technique for reducing contact and background noise in voltage spectral density measurements.," *Rev. Sci. Instrum.*, vol. 78, no. 9, p. 93905, 2007.

[13] P. Sheng, "Fluctuation-induced tunneling conduction in disordered materials," *Phys. Rev. B*, vol. 21, no. 6, pp. 2180–2195, 1980.

[14] A. Mdarhri, F. Carmona, C. Brosseau, and P. Delhaes, "Direct current electrical and microwave properties of polymer-multiwalled carbon nanotubes composites," *J. Appl. Phys.*, vol. 103, no. 5, 2008.

[15] C. Barone, S. Pagano, and H. C. Neitzert, “Effect of concentration on low-frequency noise of multiwall carbon nanotubes in high-density polyethylene matrix,” *Appl. Phys. Lett.*, vol. 97, no. 15, 2010.

[16] C. Barone, G. Landi, C. Mauro, H. C. Neitzert, and S. Pagano, “Universal crossover of the charge carrier fluctuation mechanism in different polymer/carbon nanotubes composites,” *Appl. Phys. Lett.*, vol. 107, no. 14, 2015.

[17] C. Barone, S. Pagano, and H. C. Neitzert, “Transport and noise spectroscopy of MWCNT/HDPE composites with different nanotube concentrations,” *J. Appl. Phys.*, vol. 110, no. 11, 2011.

[18] D. Tobias *et al.*, “Origins of 1⁄f noise in individual semiconducting carbon nanotube field-effect transistors,” *Phys. Rev. B*, vol. 77, no. 3, pp. 1–4, 2008.

[19] V. Podzorov, M. Uehara, M. Gershenson, T. Koo, and S. W. Cheong, “Giant 1/f noise in perovskite manganites: Evidence of the percolation threshold,” *Phys. Rev. B - Condens. Matter Mater. Phys.*, vol. 61, no. 6, pp. R3784–R3787, 2000.

[20] A. Van Der Ziel, “Noise in Solid-State Devices and Lasers,” *Proc. IEEE*, vol. 58, no. 8, pp. 1178–1206, 1970.

[21] S. T. Hsu, “Surface-State Related 1/f Noise in p-n Junctions and MOS Transistors,” *Appl. Phys. Lett.*, vol. 12, no. 9, p. 287, 1968.

[22] B. K. Jones, “Electrical Noise as a Measure of Quality and Reliability in Electronic Devices,” *Adv. Electron. Electron Phys.*, vol. 87, no. C, pp. 201–257, 1993.

[23] Z. Chobola, “Noise as a tool for non-destructive testing of single-crystal silicon solar cells,” *Microelectron. Reliab.*, vol. 41, no. 12, pp. 1947–1952, 2001.

[24] R. a Schiebel, “A model for 1/f noise in diffusion current based on surface recombination velocity fluctuations and insulator trapping,” *IEEE Trans. Electron Devices*, vol. 41, no. 5, pp. 768–778, 1994.

[25] R. MacKu and P. Koktavy, “Analysis of fluctuation processes in forward-biased solar cells using noise spectroscopy,” *Phys. Status Solidi Appl. Mater. Sci.*, vol. 207, no. 10, pp. 2387–2394, 2010.

[26] H. C. Neitzert *et al.*, “Electroluminescence efficiency degradation of crystalline silicon solar cells after irradiation with protons in the energy range between 0.8 MeV and 65 MeV,” *Phys. Status Solidi Basic Res.*, vol. 245, no. 9, pp. 1877–1883, 2008.

[27] G. Landi, C. Barone, C. Mauro, H. C. Neitzert, and S. Pagano, “A noise model for the evaluation of defect states in solar cells,” *Sci. Rep.*, vol. 6, 2016.

[28] V. Palenskis and K. Maknys, “Nature of low-frequency noise in homogeneous semiconductors,” *Sci. Rep.*, vol. 5, 2015.

[29] W. Shockley and W. T. Read, “Statistics of the recombinations of holes

and electrons," *Phys. Rev.*, vol. 87, no. 5, pp. 835–842, 1952.

[30] C. T. Sah, "The Equivalent Circuit Model in Solid-State Electronics-Part I: The Single Energy Level Defect Centers," *Proc. IEEE*, vol. 55, no. 5, pp. 654–671, 1967.

[31] G. Landi, C. Barone, A. De Sio, S. Pagano, and H. C. Neitzert, "Characterization of polymer:fullerene solar cells by low-frequency noise spectroscopy," *Appl. Phys. Lett.*, vol. 102, no. 22, 2013.

[32] S. M. Sze and K. K. Ng, *Physics of Semiconductor Devices*. 2007.

[33] S. Rein and S. W. Glunz, "Electronic properties of the metastable defect in boron-doped Czochralski silicon: Unambiguous determination by advanced lifetime spectroscopy," *Appl. Phys. Lett.*, vol. 82, no. 7, pp. 1054–1056, 2003.

[34] R. Gogolin and N. P. Harder, "Trapping behavior of Shockley-Read-Hall recombination centers in silicon solar cells," *J. Appl. Phys.*, vol. 114, no. 6, 2013.

[35] D. M. González *et al.*, "Improved Power Conversion Efficiency of P3HT:PCBM Organic Solar Cells by Strong Spin-Orbit Coupling-Induced Delayed Fluorescence," *Adv. Energy Mater.*, vol. 5, no. 8, 2015.

[36] M. Li *et al.*, "Solution-processed organic tandem solar cells with power conversion efficiencies > 12%," *Nat. Photonics*, vol. 11, no. 2, pp. 85–90, 2016.

[37] S. R. Cowan, A. Roy, and A. J. Heeger, "Recombination in polymer-fullerene bulk heterojunction solar cells," *Phys. Rev. B*, vol. 82, no. 24, p. 245207, 2010.

[38] A. De Sio *et al.*, "Solvent additives for tuning the photovoltaic properties of polymerfullerene solar cells," *Sol. Energy Mater. Sol. Cells*, vol. 95, no. 12, pp. 3536–3542, 2011.

[39] B. A. Collins, E. Gann, L. Guignard, X. He, C. R. McNeill, and H. Ade, "Molecular miscibility of polymer-fullerene blends," *J. Phys. Chem. Lett.*, vol. 1, no. 21, pp. 3160–3166, 2010.

[40] X. Yang *et al.*, "Nanoscale Morphology of High-Performance Polymer Solar Cells," *Nano Lett.*, vol. 5, no. 4, pp. 579–583, 2005.

[41] G. Perrier, R. De Bettignies, S. Berson, N. Lemaître, and S. Guillerez, "Impedance spectrometry of optimized standard and inverted P3HT-PCBM organic solar cells," *Sol. Energy Mater. Sol. Cells*, vol. 101, pp. 210–216, 2012.

[42] A. Baumann, J. Lorrmann, D. Rauh, C. Deibel, and V. Dyakonov, "A new approach for probing the mobility and lifetime of photogenerated charge carriers in organic solar cells under real operating conditions," *Adv. Mater.*, vol. 24, no. 32, pp. 4381–4386, 2012.

[43] C. Vijila *et al.*, "Relation between charge carrier mobility and lifetime in organic photovoltaics," *J. Appl. Phys.*, vol. 114, no. 18, 2013.

[44] C. Bonavolontà, C. Albonetti, M. Barra, and M. Valentino, "Electrical

mobility in organic thin-film transistors determined by noise spectroscopy," *J. Appl. Phys.*, vol. 110, no. 9, 2011.

[45] A. Pivrikas, N. S. Sariciftci, G. Juška, and R. Osterbacka, "A Review of Charge Transport and Recombination in Polymer/Fullerene Organic Solar Cells INTRODUCTION TO CHARGE CARRIER TRANSPORT IN ORGANIC SOLAR CELLS," *Photovolt Res. Appl*, vol. 15, pp. 677–696, 2007.

[46] C. Barone, G. Landi, A. De Sio, H. C. Neitzert, and S. Pagano, "Thermal ageing of bulk heterojunction polymer solar cells investigated by electric noise analysis," *Sol. Energy Mater. Sol. Cells*, vol. 122, pp. 40–45, 2014.

[47] W. S. Yang *et al.*, "Iodide management in formamidinium-lead-halide-based perovskite layers for efficient solar cells," *Science (80-.).*, vol. 356, no. 6345, pp. 1376–1379, 2017.

[48] M. A. Green, A. Ho-Baillie, and H. J. Snaith, "The emergence of perovskite solar cells," *Nature Photonics*, vol. 8, no. 7. pp. 506–514, 2014.

[49] C. Wehrenfennig, M. Liu, H. J. Snaith, M. B. Johnston, and L. M. Herz, "Charge-carrier dynamics in vapour-deposited films of the organolead halide perovskite $CH_3NH_3PbI_{3-x}Cl_x$," *Energy Environ. Sci.*, vol. 7, no. 7, pp. 2269–2275, 2014.

[50] C. D. Bailie *et al.*, "Semi-transparent perovskite solar cells for tandems with silicon and CIGS," *Energy Environ. Sci.*, vol. 8, no. 3, pp. 956–963, 2015.

[51] P. Löper *et al.*, "Organic–inorganic halide perovskite/crystalline silicon four-terminal tandem solar cells," *Phys. Chem. Chem. Phys.*, vol. 17, no. 3, pp. 1619–1629, 2015.

[52] G. Divitini, S. Cacovich, F. Matteocci, L. Cinà, A. Di Carlo, and C. Ducati, "In situ observation of heat-induced degradation of perovskite solar cells," *Nat. Energy*, vol. 1, no. 2, p. 15012, 2016.

[53] C. Eames, J. M. Frost, P. R. F. Barnes, B. C. O'Regan, A. Walsh, and M. S. Islam, "Ionic transport in hybrid lead iodide perovskite solar cells," *Nat. Commun.*, vol. 6, p. 7497, 2015.

[54] Y. Shao, Z. Xiao, C. Bi, Y. Yuan, and J. Huang, "Origin and elimination of photocurrent hysteresis by fullerene passivation in CH3NH3PbI3planar heterojunction solar cells," *Nat. Commun.*, vol. 5, 2014.

[55] C. Wehrenfennig, G. E. Eperon, M. B. Johnston, H. J. Snaith, and L. M. Herz, "High charge carrier mobilities and lifetimes in organolead trihalide perovskites," *Adv. Mater.*, vol. 26, no. 10, pp. 1584–1589, 2014.

[56] J. Even, L. Pedesseau, and C. Katan, "Analysis of multivalley and multibandgap absorption and enhancement of free carriers related to exciton screening in hybrid perovskites," *J. Phys. Chem. C*, vol. 118, no. 22, pp. 11566–11572, 2014.

[57] B. Yang *et al.*, "Low Threshold Two-photon-pumped Amplified Spontaneous Emission in CH3NH3PbBr3 Microdisks," *ACS Appl. Mater. Interfaces*, vol. 8, pp. 6–11, 2016.

[58] T. Baikie *et al.*, “Synthesis and crystal chemistry of the hybrid perovskite (CH3NH3)PbI3 for solid-state sensitised solar cell applications,” *J. Mater. Chem. A*, vol. 1, no. 18, p. 5628, 2013.

[59] E. L. Unger *et al.*, “Hysteresis and transient behavior in current–voltage measurements of hybrid-perovskite absorber solar cells,” *Energy Environ. Sci.*, vol. 7, no. 11, pp. 3690–3698, 2014.

[60] J. H. Heo, H. J. Han, D. Kim, T. K. Ahn, and S. H. Im, “Hysteresis-less inverted CH 3 NH 3 PbI 3 planar perovskite hybrid solar cells with 18.1% power conversion efficiency,” *Energy Environ. Sci.*, vol. 8, no. 5, pp. 1602–1608, 2015.

[61] Q. Dong *et al.*, “Electron-hole diffusion lengths > 175 μm in solution-grown CH3NH3PbI3 single crystals,” *Science (80-.).*, vol. 347, no. 6225, pp. 967–970, 2015.

[62] S. D. Stranks *et al.*, “Electron-hole diffusion lengths exceeding 1 micrometer in an organometal trihalide perovskite absorber,” *Science (80-.).*, vol. 342, no. 6156, pp. 341–344, 2013.

[63] H. Zhang *et al.*, “Photovoltaic behaviour of lead methylammonium triiodide perovskite solar cells down to 80 K,” *J. Mater. Chem. A*, vol. 3, no. 22, pp. 11762–11767, 2015.

[64] P. Delugas, A. Filippetti, and A. Mattoni, “Methylammonium fragmentation in amines as source of localized trap levels and the healing role of Cl in hybrid lead-iodide perovskites,” *Phys. Rev. B - Condens. Matter Mater. Phys.*, vol. 92, no. 4, 2015.

[65] V. V. Brus *et al.*, “Defect Dynamics in Proton Irradiated CH3NH3PbI3 Perovskite Solar Cells,” *Adv. Electron. Mater.*, vol. 3, no. 2, 2017.

[66] Z. Pomerantz, A. Zaban, S. Ghosh, J. P. Lellouche, G. Garcia-Belmonte, and J. Bisquert, “Capacitance, spectroelectrochemistry and conductivity of polarons and bipolarons in a polydicarbazole based conducting polymer,” *J. Electroanal. Chem.*, vol. 614, no. 1–2, pp. 49–60, 2008.

[67] J. Bisquert, G. Garcia-Belmonte, and J. García-Cañadas, “Effects of the Gaussian energy dispersion on the statistics of polarons and bipolarons in conducting polymers,” *J. Chem. Phys.*, vol. 120, no. 14, pp. 6726–6733, 2004.

[68] Y. Shao, Y. Yuan, and J. Huang, “Correlation of energy disorder and open-circuit voltage in hybrid perovskite solar cells,” *Nat. Energy*, vol. 1, no. 1, p. 15001, Jan. 2016.

[69] G. Landi *et al.*, “Correlation between Electronic Defect States Distribution and Device Performance of Perovskite Solar Cells,” *Adv. Sci.*, vol. 4, no. 10, 2017.

[70] M. Samiee *et al.*, “Defect density and dielectric constant in perovskite solar cells,” *Appl. Phys. Lett.*, vol. 105, no. 15, 2014.

[71] G. D. Cody, T. Tiedje, B. Abeles, B. Brooks, and Y. Goldstein, “Disorder and the optical-absorption edge of hydrogenated amorphous silicon,” *J. Phys.*

Colloq., vol. 42, no. 10, pp. c4-301, 1981.

[72] S. Singh *et al.*, "Effect of Thermal and Structural Disorder on the Electronic Structure of Hybrid Perovskite Semiconductor CH3NH3PbI3," *J. Phys. Chem. Lett.*, vol. 7, pp. 3014–3021, 2016.

[73] S. D. Stranks and H. J. Snaith, "Metal-halide perovskites for photovoltaic and light-emitting devices," *Nature Nanotechnology*, vol. 10, no. 5. pp. 391–402, 2015.

[74] R. M. Gibb *et al.*, "V. A two stage model for deep level capture," *Philos. Mag.*, vol. 36, no. 4, pp. 1021–1034, 1977.

[75] C. Barone *et al.*, "Unravelling the low-temperature metastable state in perovskite solar cells by noise spectroscopy," *Sci. Rep.*, vol. 6, 2016.

List of publications and presentation

Published papers

1) C. Barone, G. Landi, C. Mauro, H. C. Neitzert, and S. Pagano, “Universal crossover of the charge carrier fluctuation mechanism in different polymer/carbon nanotubes composites”, Appl. Phys. Lett., vol. 107, no. 14, 2015.
2) C. Barone, G. Landi, C. Mauro, S. Pagano, and H. C. Neitzert, “Low-frequency electric noise spectroscopy in different polymer/carbon nanotubes composites”, Diam. Relat. Mater., vol. 65, pp. 32–36, 2016.
3) G. Landi, C. Barone, C. Mauro, H. C. Neitzert, and S. Pagano, “A noise model for the evaluation of defect states in solar cells”, Sci. Rep., vol. 6, 2016.
4) C. Barone, F. Lang, C. Mauro, G. Landi, J. Rappich, N. H. Nickel, B. Rech, S. Pagano, and H. C. Neitzert, “Unravelling the low-temperature metastable state in perovskite solar cells by noise spectroscopy”, Sci. Rep., vol. 6, 2016.
5) C. Mauro, C. Barone, S. Pagano, Y. Imai, F. Nabeshima, and A. Maeda, “Noise Spectroscopy Investigation of Aging-Induced Degradation in Iron-Chalcogenide Superconductors”, IEEE Trans. Appl. Supercond., vol. 27, no. 4, 2017.
6) G. Landi, H. C. Neitzert, C. Barone, C. Mauro, F. Lang, S. Albrecht, B. Rech, and S. Pagano, “Correlation between Electronic Defect States Distribution and Device Performance of Perovskite Solar Cells”, Adv. Sci., vol. 4, no. 10, 2017.
7) G. Landi, C. Barone, C. Mauro, A De Sio, G. Carapella, H. C. Neitzert, and S. Pagano, “Probing temperature-dependent recombination kinetics in polymer: Fullerene solar cells by electric noise spectroscopy”, Energies, vol. 10, no. 10, 2017.
8) C. Barone, C. Mauro, G. Carapella, and S. Pagano, “Noise Level Comparison in Novel Superconducting Materials”, 16th Int. Supercond. Electron. Conf., vol. 1, pp. 8–10, 2017.
9) G. Landi, C. Barone, C. Mauro, S. Pagano, and H.C. Neitzert, "Evaluation of silicon, organic, and perovskite solar cell reliability with low-frequency noise spectroscopy", IEEE Conf. Proc. -, 6C.3-1, 2018

Conferences

1) International Conference on Diamond and Carbon Materials 2015 (Bad Homburg [Germany], 06-10/09/2015): POSTER PRESENTED "Low-frequency electric noise spectroscopy in different polymer/carbon nanotubes composites"
2) 2016 Applied Superconductivity Conference (Denver [U.S.A.], 04-09/09/2016): POSTER PRESENTED "Noise Spectroscopy Investigation of Aging-Induced Degradation in Iron-Chalcogenide Superconductors"
3) International Superconductive Electronics Conference ISEC 2017 (Sorrento [Italy], 12-16/06/2017): POSTER PRESENTED "Comparison of the Electric Noise Properties of Novel Superconductive Materials for Electronics Applications"